Investigation of the spatially anisotropic component of the laterally averaged molecular hydrogen/Ag(111) physisorption potential

K. Birgitta Whaley,[a] Chien-fan Yu,[b] Charles S. Hogg, John C. Light, and Steven J. Sibener[c]
Department of Chemistry and The James Franck Institute, The University of Chicago, Chicago, Illinois 60637

(Received 13 February 1985; accepted 31 May 1985)

A detailed investigation of the spatially anisotropic component of the laterally averaged molecular hydrogen/Ag(111) physisorption potential is presented. Experimentally derived rotationally inelastic transition probabilities for H_2, D_2, and HD, taken as a function of collision energy, are compared with those resulting from close-coupled quantum scattering calculations. These calculations utilize exponential-3 and variable exponent parametrizations of the laterally averaged isotropic potential which reproduce the experimental bound state resonance spectra for p-H_2 and o-D_2 on Ag(111). Complementary information is obtained by analyzing the magnetic sublevel splittings for physisorbed $J = 1$ n-H_2, using diffractive selective adsorption resonance energies calculated with first order perturbation theory. Theoretical predictions for HD/Ag(111) rotationally mediated selective adsorption resonances are also compared with previously reported experimental results, which show well resolved J-dependent energy shifts resulting in part from the orientational anisotropy of the potential. The results obtained in this study indicate that both the attractive and repulsive parts of the anisotropic potential exhibit only a weak orientation dependence, in agreement with recent theoretical predictions for this system.

I. INTRODUCTION

Until recently, the physisorptive interaction of molecules with surfaces was far less extensively investigated than that of atoms with surfaces. Diffractive selective adsorption experiments which have been carried out with molecules, such as those involving H_2 and D_2 on LiF, NiO, graphite, and stepped surfaces of copper,[1] were typically analyzed to obtain bound states of the laterally averaged interaction potential with the molecule treated as a structureless particle. Recent advances in molecular beam surface scattering experimentation have now prompted a growing interest in the role of the internal molecular degrees of freedom in molecule–surface interactions. This has been evidenced by a large number of experimental and theoretical studies of rotationally and vibrationally inelastic molecule–surface collision systems.[2]

A prime objective in these studies is the determination of the molecule–surface interaction potential. Because of the molecular orientation dependence this is considerably more complicated for a molecule–surface collision than for atom–surface collisions. For a diatomic molecule incident upon a perfectly periodic surface, the molecule–surface interaction potential may be written as the Fourier sum

$$V(z,\theta,\phi,\mathbf{R},r) = \sum_{\mathbf{G}} V_{\mathbf{G}}(z,\theta,\phi,r)e^{i\mathbf{G}\cdot\mathbf{R}}, \tag{1.1}$$

where z is the normal distance from the molecule center of mass to the surface, $\mathbf{R} = (x,y)$ is the surface projection of the center of mass relative to some origin on the surface, θ and ϕ are the polar and azimuthal orientation angles of the molecular orientation in the xyz frame, and r is the molecular internuclear distance (Fig. 1). We shall be concerned with low energy (< 150 meV) collisions of the molecular hydrogen isotopes for which a rigid rotor assumption is valid. The

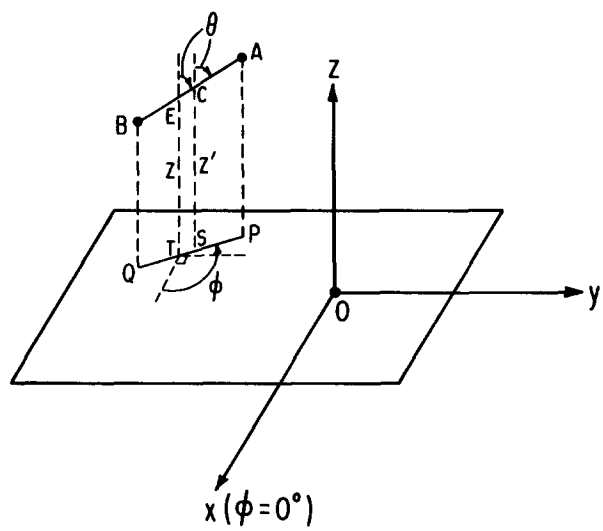

FIG. 1. Coordinate system for a diatomic molecule AB incident upon a stationary corrugated surface. O is the origin of coordinates, fixed at some reference point in the surface unit cell, C the midpoint of the internuclear distance AB (i.e., the center of geometry), E the molecular center of mass. PQ is the projection of AB in the surface xy plane, S and T are the projections of C and E, respectively. The locations of C and E in the xyz frame are thus given by vectors $(\mathbf{R}',z')$ and $(\mathbf{R},z)$, respectively, where $\mathbf{R} = (x,y)$. Atoms A and B have masses m_1 and m_2 and coordinates $(\mathbf{R}_2,z_1)$ and $(\mathbf{R}_2,z_2)$, respectively. The internal degrees of freedom are expressed in the spherical polar coordinates (r,θ,ϕ) where r is the internuclear distance AB, and θ and ϕ the polar and azimuthal angles, measured in the xyz frame. EC, the offset of the center of mass from the center of geometry, is denoted by δ and is equal in magnitude to $r(m_1 - m_2)/2(m_1 + m_2)$.

[a] Current address: Dept. of Chemistry, Tel Aviv Univeristy, Israel.
[b] Current address: Dept. of Chemistry, Columbia University, New York.
[c] Alfred P. Sloan Research Fellow.

laterally averaged potential $V_{00}(z,\theta,\phi,r)$ can then only be a function of z and θ, since physically there can be no azimuthal orientation dependence for a diatomic interacting with a flat surface. Changes in rotational polarization or rotational state selected molecules can only arise from the presence of higher order diffractive terms ($G \neq 0$) in Eq. (1.1). [However, matrix elements of the laterally averaged potential $V_{00}(z,\theta)$ will be different for different magnetic quantum states of the diatom, with the result that an overall apparent change in rotational polarization may be produced by scattering an initial ensemble of $|Jm\rangle$ molecules from a flat surface.[3]] We restrict our attention here to the laterally averaged potential $V_{00}(z,\theta)$: this is the component probed by rotationally inelastic scattering from smooth surfaces and by selective adsorption resonance phenomena on weakly corrugated surfaces.

Several electron energy loss spectroscopy (EELS) and molecular beam scattering experiments recently carried out for the adsorption of molecular hydrogen on smooth metal surfaces indicate that the physisorbed molecule behaves as a nearly free three-dimensional rotor, with only weak perturbations due to the anisotropy of the (laterally averaged) molecule–surface interaction.[4,5] However, the low energy resolution currently available in EELS experiments ($\gtrsim 3$ meV) limits the capability of this technique for investigating the exact nature of the physisorbed state at the present time. We have recently reported a detailed comprehensive study of the diffractive selective adsorption (hereafter, DSA) in the molecular beam scattering of n-H_2, p-H_2, n-D_2, and o-D_2 from Ag(111) which shows evidence of small $|J,m\rangle$-dependent shifts in the bound states of $V_{00}(z,\theta)$, arising from the weak anisotropic component of this potential.[6] This was made possible by the high energy resolution of these molecular beam experiments ($\sim 200\ \mu$eV) and the development of a pure $J=0$ hydrogen beam. Such shifts have also recently been observed for n-H_2 on the more strongly corrugated Ag(110) surface.[7] Similar J-dependent shifts are apparent in the recent measurements of rotationally mediated selective adsorption (henceforth, RMSA) resonances, for HD on Pt(111)[8] and for HD on Ag(111).[9]

These selective adsorption studies are part of a detailed experimental and theoretical study of the molecular hydrogen/Ag(111) physisorption interaction potential, including the laterally averaged isotropic, the laterally averaged anisotropic, and the higher order periodic components. The laterally averaged isotropic component has been treated in previous publications[6,10] while the periodic potential will be presented elsewhere.[11] It is the purpose of this paper to investigate the anisotropic component of $V_{00}(z,\theta)$ in considerable detail for the molecular hydrogen isotopes/Ag(111) system, employing a combination of experimental measurements and theoretical calculations.

A comprehensive study of the molecular beam scattering of hydrogen from Ag(111) carried out in our laboratory has yielded the following array of information: rotationally inelastic and elastic transition probabilities for H_2, D_2, and HD, RMSA resonances for HD and isolated instances of RMSA resonances for H_2 and D_2, and DSA resonances for H_2 and D_2 in which $|J,m\rangle$-dependent shifts and linewidth differences (for H_2) are seen between n-H_2 and p-H_2, and n-D_2 and o-D_2, respectively. Transition probabilities for simultaneous diffractive and rotationally inelastic excitation of HD, and for diffraction and diffraction-rotation excitation of H_2 and D_2 have also been measured.

From an experimental point of view the low energy scattering of molecular hydrogen from Ag(111) is a prime example for which to attempt an empirical analysis of the physisorptive interaction potential. The extremely low corrugation of this surface facilitates the analysis of DSA resonances since complications due to band structure are not present. The smoothness of this surface also concentrates the final scattering intensities in the specular channel. Molecular hydrogen does not dissociatively chemisorb on Ag(111), thereby allowing cryogenically cooled targets to be used and minimizing Debye–Waller attenuation. H_2, D_2, and HD are excellent candidates for study in the sense that only a small number of final inelastic scattering channels are energetically accessible. Theoretically, this also makes potential variation within the context of close coupled calculations feasible, which enables one to take full advantage of the information in the selective adsorption resonances and inelastic transition probabilities. The relatively large rotational spacings of these molecules also allow the final rotational state populations to be probed by measuring outgoing angular distributions, alleviating the need for a laser-based detection system. Finally, it is also worth noting that although HD/Ag(111) is the richest system in terms of large rotational inelasticity and producing strong RMSA resonances, H_2 and D_2 actually provide a more sensitive probe of the anisotropy of $V_{00}(z,\theta)$. This interesting situation arises since the HD rotational transitions and J-dependent RMSA energy shifts are primarily governed by the mass asymmetry of the molecule, which is large enough to obscure the subtle effects which are due to the weak anisotropy of the potential. Such problems do not arise when similar measurements are performed with the homonuclear isotopes H_2 and D_2.

The problem of inversion of a multiple component potential such as $V_{00}(z,\theta)$ presents a major theoretical challenge. In the absence of good inversion procedures we adopt here an empirical approach, taking a suitable parametric form for $V_{00}(z,\theta)$ and then performing quantum close coupled scattering calculations to obtain transition probabilities and resonance shifts in agreement with experiment. The rotational transition probabilities and the resonance energies provide *complementary* information on the interaction potential which will prove to be essential for an unambiguous determination of the anisotropy of the interaction. We proceed stepwise by assuming the previously established isotropic component $V_{00}^{0}(z)$[6,10] and consider here only the remaining parametrization of the anisotropic component.

Finally, hydrogenic systems are also simple enough that *ab initio* theoretical estimates of the interaction potential can be made and asymptotic expressions for both attractive and repulsive terms of the anisotropic component of $V_{00}(z,\theta)$ are available for comparison.[12,13]

The plan of the remainder of the paper is as follows. In Sec. II we discuss the theoretical basis for a single functional form of the laterally averaged potential and outline the theo-

retical procedure to be followed in the investigation of the potential. Section III contains a summary of the experimental procedures for obtaining rotationally inelastic transition probabilities, resonance energies, and associated linewidth information. In Sec. IV the rotationally inelastic scattering data and data analysis for H_2 and D_2 are presented, followed by the results of scattering calculations. In Sec. V the selective adsorption resonances for n-H_2, p-H_2, n-D_2, and o-D_2 are discussed: linewidth broadening of n-H_2 due to averaging over $|J,m\rangle$ components of the initial beam and shifts of n-H_2 resonances relative to p-H_2 are analyzed. The analysis in each of these sections yields a set of possible parametrizations of the anisotropy and the intersection of these two sets gives us a unique parameter set. In Sec. VI we present the rotational transition probabilities for the HD scattering and compare the HD RMSA resonance energies and transition probabilities with the theoretical predictions from the best fit anisotropy obtained from the H_2 and D_2 data. Finally, Sec. VII contains a discussion of the results, a summary, and our concluding remarks.

II. THEORY

A. The laterally averaged interaction potential

The laterally averaged interaction potential for a rigid rotor, $V_{00}(z,\theta)$, may be written as the sum of an attractive long range polarization potential and a repulsive short range potential deriving from overlap of molecular and solid electronic wave functions. In general, each of these terms will have a different orientation dependence:

$$V_{00}(z,\theta) = V_{00,R}(z,\theta) + V_{00,A}(z,\theta). \tag{2.1}$$

Ab initio theoretical calculation of each of these components is rendered exceedingly difficult by the many body nature of the interaction and, for metals, also by the delocalization of the electron density. However, asymptotic expressions have recently been derived which give rise to simple few parameter functional forms. For the van der Waals interaction

$$V_{00,A}(z,\theta) \sim \frac{-C_3(\theta)}{z^3}, \tag{2.2}$$

where the orientation dependence of $C_3(\theta)$ arises as a result of the anisotropy of the molecular polarizability. For a homonuclear diatomic molecule it is given by[12]

$$C_3(\theta) = C_3^{(0)} + C_3^{(2)} P_2(\cos\theta). \tag{2.3}$$

Harris and Feibelman have obtained $C_3^{(2)} \sim 0.05 C_3^{(0)}$ for H_2.[12] The repulsive component has been estimated by Harris and Liebsch from consideration of the effective orthogonalization of the molecular and metal electron wave functions as[13]

$$V_{00,R}(z,\theta) \sim A e^{-k_\Phi z}\left\{1 + \frac{r_e^2 k_\Phi^2}{12}[1 + 2P_2(\cos\theta)]\right\}, \tag{2.4}$$

where $k_\Phi = (2m_e\Phi/\hbar^2)^2$ is the decay constant of a Fermi-surface Bloch wave function (Φ is the work function, m_e the electron mass) and r_e the molecular internuclear distance.

These estimates give a laterally averaged interaction potential with two parameters β_A and β_R specifying the anisotropy

$$V_{00}(z,\theta) = v_{00,R}(z)[1 + \beta_R P_2(\cos\theta)] + v_{00,A}(z) \times [1 + \beta_A P_2(\cos\theta)] \tag{2.5}$$

$$= v_{00}^0(z) + v_{00}^2(z) P_2(\cos\theta). \tag{2.6}$$

Using the appropriate parameters for H_2/Ag(111) ($r_e = 1.4a_0$, $\Phi = 4.24$ eV we find $\beta_R \sim 0.10$ from Eq. (2.4) and $\beta_A \sim 0.06$ from Eq. (13) of Ref. 12, using accurate values of the polarizability tensor of H_2.[14] Both β_A and β_R are positive, reflecting the asymptotically preferred perpendicular orientation at large z and parallel orientation at small z. Equations (2.5) and (2.6) form the basis of the parametrizations used in our studies. We shall use two different isotropic potentials:

$$v_{00}^0(z) = v_{00,R}(z) + v_{00,A}(z) \tag{2.7}$$

and obtain the anisotropic term $v_{00}^2(z)$ from Eq. (2.5) as the linear combination

$$v_{00}^2(z) = \beta_R v_{00,R}(z) + \beta_A v_{00,A}(z). \tag{2.8}$$

Thus β_A and β_R can be regarded as parameters which allow independent variation of the attractive and repulsive components, respectively, with regard to the molecular orientation. Equation (2.8) is an improvement over the one parameter anisotropy previously used to study rotationally inelastic scattering of HD from Ag(111).[9] The anisotropy is thus determined both by the parameters β_A, β_R *and* by the functional form of the isotropic potential $v_{00}^0(z)$.

For $v_{00}^0(z)$ we use (i) the variable exponent potential (hereafter VEP)

$$v_{00}^0(z) = D\{[1 + (\lambda/p)(z - z_e)]^{-2p} - 2[1 + (\lambda/p)(z - z_e)]^{-p}\} \tag{2.9}$$

and (ii) the exponential-3 potential (hereafter exp-3)

$$v_{00}^0(z) = \left(\frac{D\alpha z_e}{\alpha z_e - 3}\right)\left[\frac{3}{\alpha z_e} e^{-\alpha(z - z_e)} - \left(\frac{z_e}{z}\right)^3 f(z)\right], \tag{2.10}$$

$$f(z) = 1 - [2(z/a_0)(z/a_0 + 1) + 1]\exp(-2z/a_0), \tag{2.11}$$

where $f(z)$ is a cutoff function going smoothly from $f(0) = 0$ to $f(z) = 1$ at large z. The VEP is a flexible three parameter potential with semianalytic eigenvalues[15] which has been used to fit the bound state levels of laterally averaged physisorption potentials for atom–surface systems.[16] The exponential-3 potential has the form predicted by the *ab initio* theoretical studies, Eqs. (2.2)–(2.4), but is somewhat more difficult to work with, having no analytic eigenvalues and requiring a cutoff function to remove the singularity at $z = 0$.

Equation (2.7) with both Eqs. (2.9) and (2.10) is approximate in that it neglects correlation between metal and electronic wave functions. A consequence of the use of the asymptotic results for $V_{00,A}(z,\theta)$ *and* $V_{00,R}(z,\theta)$ [Eqs. (2.2)–(2.4)] is that the z dependence of $v_{00}^2(z)$ is determined by that of the components $v_{00,R}(z)$ and $v_{00,A}(z)$ of $v_{00}^0(z)$. The calculations presented in Sec. IV will show that this form cannot entirely account for the energy dependence of the transition probabilities. An analogous situation is seen in diffractive scattering of atoms from surfaces.[17] We have therefore also briefly considered the introduction of a third parameter into

$v_{00}^2(z)$ which modifies the softness of the repulsive component:

$$v_{00}^2(z) = \beta_R \exp(-\alpha_2 z) v_{00,R}(z) + \beta_A v_{00,A}(z). \quad (2.12)$$

The above discussion based on Eq. (2.5) refers to the interaction potential for a homonuclear molecule. The interaction potential for HD in the center of mass coordinates (z,θ) is then obtained from that for H_2 [Eq. (2.5)] by the transformation

$$z = z' - \delta \cos\theta \quad (2.13)$$

with Eq. (2.5) valid for (z',θ). Thus for HD we obtain

$$\tilde{V}_{00}(z,\theta) = V_{00}(z',\theta) \quad (2.14)$$

$$= v_{00}^0(z + \delta\cos\theta) + v_{00}^2(z + \delta\cos\theta) P_2(\cos\theta) \quad (2.15)$$

$$= v_{00}^0(z) + \sum_{l=0,1,2,\ldots} \tilde{v}_{00}^l(z) P_l(\cos\theta) \quad (2.16)$$

with $\delta = r_e/6$, and where r_e is the equilibrium internuclear distance. The resulting potential, denoted $\tilde{V}_{00}(z,\theta)$ to distinguish it from the homonuclear case, now contains odd order Legendre terms, reflecting the absence of the $\Delta J = 0,2$ selection rule for the asymmetric species. The separation of the zeroth order term into $v_{00}^0(z)$ and $\tilde{v}_{00}^0(z)$ is convenient in order to be able to refer to the resonance states (both DSA and RMSA) of all isotopic variants in the same terms (Secs. V and VI).

B. Theoretical analysis of transition probabilities and resonance data

It is clear that rotational transition probabilities and selective adsorption resonance data provide independent, and in some sense complementary, information on the anisotropic component $v_{00}^2(z)$ of the interaction potential. The rotational transition probabilities probe the anisotropic component at small z values near the turning point of $v_{00}^0(z)$ and will be determined both by β_R and β_A. At high incident energies the β_R dependence may be expected to be stronger than the β_A dependence but in general the precise balance will be dependent on the form of the isotropic potential components $v_{00,R}(z)$ and $v_{00,A}(z)$. The resonances are determined primarily by the isotropic potential $v_{00}^0(z)$: information on the anisotropic component in the region of the bound levels of $v_{00}^0(z)$ is obtained from the $|Jm\rangle$-dependent shifts and linewidth differences seen, for example, for n-H_2 and p-H_2. Since the form of $v_{00}^2(z)$ in the region of the minimum of $v_{00}^0(z)$ is strongly dependent upon the combination of β_A, β_R, these shifts and linewidths will be very sensitive to simultaneous variations in both β_A *and* β_R.

We first discuss the rotational transition probabilities. The rotational inelasticity of HD is considerably larger than that of H_2 and D_2 as a result of the asymmetry introduced by the offset of the center of mass, δ [Eq. (2.13)]. However, as a consequence the dependence of rotational inelastic probabilities on the relatively weak orientational anisotropy deriving from $v_{00}^2(z)$ is masked by the effect of this center of mass asymmetry. Far more sensitive to β_A and β_R are the H_2 and D_2 rotational transition probabilities as a function of incident perpendicular energy $E_{z_i} = E_b \cos^2\theta_i$ where E_b is the beam energy and θ_i is the incident beam angle from the surface normal. The experimentally measured ratio of probabilities $P(J=0\to 2)/P(J=0\to 0)$ for H_2 and D_2 is thus the quantity which will be compared with the transition probability ratio derived from close coupling calculations in order to extract a first quantitative estimate of β_A, β_R for a given $v_{00}^0(z)$. Note that the relatively large HD rotational transition probabilities are nevertheless dependent upon gross features of the isotropic potential $v_{00}^0(z)$, such as the well depth. This was utilized in our previous study of the isotropic component of $V_{00}(z,\theta)$.[10]

In the first approximation DSA resonance energies are given by eigenvalues of $v_{00}^0(z)$ plus the kinetic energy parallel to the surface obtained by transfer of a reciprocal lattice vector $\mathbf{G}$ to the incident parallel momentum $\mathbf{K}_i$. Similarly, RMSA resonance energies are given to a first approximation by the bound vibration–rigid rotor (BVRR) energies,[18] which are eigenvalues of $v_{00}^0(z)$ plus free rotor energies. Shifts from these zeroth order DSA resonance energies, and from the BVRR energies, arise from the anisotropic component of $V_{00}(z,\theta)$ and result in the experimentally observed $|Jm\rangle$ and J dependence of bound levels extracted from DSA and RMSA measurements, respectively.

The connection between the two kinds of resonances is clearly seen from the standard set of close coupled equations resulting from a product basis expansion in rigid rotor and diffraction states with

$$H = \frac{\hbar^2}{2M}\nabla^2 - \frac{\hbar^2}{2I}\left[\frac{1}{\sin\theta}\frac{\partial}{\partial\theta}\sin\theta\frac{\partial}{\partial\theta}\right] + V_{00}(z,\theta), \quad (2.17)$$

$$\psi(z,\theta,\phi,\mathbf{R}) = \sum_{\mathbf{G}Jm} \chi_{\mathbf{G}Jm}(z)\, Y_{Jm}(\theta,\phi) e^{i(\mathbf{K}_i+\mathbf{G})\cdot\mathbf{R}} \quad (2.18)$$

we obtain

$$\left\{\frac{d^2}{dz^2} + k_{\mathbf{G}J}^2\right\}\chi_{\mathbf{G}Jm}(z) = \sum_{J'} \frac{2M}{\hbar^2}\langle Jm|V_{00}(z,\theta)|J'm\rangle \chi_{\mathbf{G}J'm}(z), \quad (2.19)$$

$$k_{\mathbf{G}J}^2 = \frac{2M}{\hbar^2}E - (\mathbf{K}_i + \mathbf{G})^2 - \frac{M}{I}J(J+1). \quad (2.20)$$

For atoms or spherical molecules $V_{00}(z,\theta)$ reduces to $v_{00}^0(z)$ and the resonance condition is then

$$E = \frac{\hbar^2}{2M}(\mathbf{K}_i + \mathbf{G})^2 + \frac{\hbar^2}{2I}J(J+1) + \epsilon_n \quad (2.21)$$

with ϵ_n a negative eigenvalue of $v_{00}^0(z)$. Equation (2.21) is the generalization of the zeroth order atom–surface DSA resonance condition and can be regarded as representing a diffractive and rotationally excited molecular state in which the molecule moves freely parallel to the surface but is in a bound vibrational state perpendicular to the surface with energy $\epsilon_n < 0$. We refer to these energies as BVRR energies, for both zero and nonzero $\mathbf{G}$.

In general the set of coupled equations (2.19) must be solved exactly for each $\mathbf{G}$ and m in order to find the resonance energies. However, when the anisotropy is small the resonances may be found by perturbation theory.[18] Thus for the homonuclear diatom–surface systems, application of

first order perturbation theory to Eq. (2.19) gives resonance energies

$$E = \frac{\hbar^2}{2M}(\mathbf{K}_i + \mathbf{G})^2 + \frac{\hbar^2}{2I}J(J+1) + \epsilon_n + \epsilon^{(1)}_{n,Jm}, \quad (2.22)$$

where

$$\epsilon^{(1)}_{n,Jm} = \langle n|v^2_{00}(z)|n\rangle\langle Jm|P_2(\cos\theta)|Jm\rangle \quad (2.23)$$

while for the heteronuclear case we have Eq. (2.22) with $\epsilon^{(1)}_{n,Jm}$ replaced by $\tilde{\epsilon}^{(1)}_{n,Jm}$:

$$\tilde{\epsilon}^{(1)}_{n,Jm} = \sum_{l=0,1,2\ldots} \langle n|\tilde{v}^l_{00}(z)|n\rangle\langle Jm|P_l(\cos\theta)|Jm\rangle. \quad (2.24)$$

Equation (2.22) is the kinematic resonance condition for a mixed DSA-RMSA resonance to first order in the anisotropic component of $V_{00}(z,\theta)$. Pure RMSA or pure DSA resonances are obtained by setting $\mathbf{G}$ or J equal to zero, respectively (if the initial state is rotationally excited, pure DSA is obtained when $\Delta J = 0$).

$\epsilon^{(1)}_{n,Jm}$ and $\tilde{\epsilon}^{(1)}_{n,Jm}$ are the first order $|Jm\rangle$- and n-dependent shifts from the BVRR energies [Eq. (2.21)] for the homonuclear and heteronuclear adsorbed molecular species, respectively. Equations (2.22) and (2.24) show that *even in the absence of an anisotropic term* $v^2_{00}(z)$, the observed HD RMSA resonance energies will show $|Jm\rangle$-dependent shifts for a given bound state n. The fact that the observed J-dependent shifts seen in HD RMSA resonance measurements on both Pt(111)[8] and Ag(111)[9] (for $m = 0$) are much larger than the $|J\rangle$-dependent shifts seen in H_2 and D_2 DSA RMSA measurements on Ag(111)[6] (~ 1.0 meV for HD, compared to ~ 0.2 meV for H_2 and D_2) is not surprising in view of the large asymmetry of HD. Thus just as with the rotational transition probabilities, the high anisotropy induced by the asymmetry of HD masks the potential anisotropy from $v^2_{00}(z)$ and renders the RMSA resonance shifts for HD less sensitive to small changes in $v^2_{00}(z)$ than the DSA and RMSA resonance shifts for H_2 and D_2.

Provided first order perturbation theory is a valid description of the resonances, then an adsorbed ground state molecule $|Jm\rangle = |00\rangle$ will have zero shift $\epsilon^{(1)}_{n,Jm}$ (or $\tilde{\epsilon}^{(1)}_{n,Jm}$) and yields the true bound state energies, ϵ_n, of $v^0_{00}(z)$. This forms the basis of the empirical determination of the isotropic component of $V_{00}(z,\theta)$ from DSA measurements of p-H_2 and o-D_2 on Ag(111) which was reported previously.[10] (Note that adsorbed $J = 0$ can not be observed in RMSA resonances, by definition.) We should emphasize that because the bound state energies determined for $|J,m\rangle = |0,0\rangle$ are independent of the anisotropic potential, $v^0_{00}(z)$ may be determined first, and then the anisotropic components may be determined, without the need for iteration.

For a given bound level n, the first order resonance shifts $\epsilon^{(1)}_{n,Jm}$ provide direct information on the anisotropic component, $v^2_{00}(z)$. Any well resolved selective adsorption resonance which is unambiguously assignable to a single $|Jm\rangle$ rotor state will give rise to a set of possible pairs of parameters β_A, β_R via Eqs. (2.8) and (2.23). Resonances observed for n-H_2 and n-D_2 will reflect an average over $|Jm\rangle$ states $|0,0\rangle$, $|1,0\rangle$, and $|1,\pm 1\rangle$ [$\pm m$ have equal shifts according to Eq. (2.23)], with appropriate weightings resulting from the nuclear statistics. Unfortunately the resolution in the present experiments ($\sim 250\,\mu$eV) is too low to resolve the individual multiplet components for the normal hydrogen isotopes in the extremely weak DSA resonance dips observed in the specular scattering from Ag(111). On the more strongly corrugated Ag(110) surface where the resonance structure is stronger, there is some evidence for a splitting of the n-H_2 DSA resonances.[7,19] In our experiments on Ag(111) we do, however, observe (i) an averaged effective shift of the resonance energy for n-H_2 from that for p-H_2 (and n-D_2 from o-D_2) and (ii) a distinct *linewidth broadening* for n-H_2 and n-D_2 relative to p-H_2 and o-D_2, respectively.[6] Both the effective shift and the linewidth broadening may be simulated as a function of the parameters β_A, β_R, using a natural linewidth for the $|Jm\rangle$ states obtained from the measured linewidth of p-H_2 and o-D_2.

Each of these comparisons between experiment and theoretical simulation, i.e., for transition probabilities and for resonance shifts, will provide a set of parameter pairs β_A, β_R. We regard the intersection of these two sets as providing the correct parameters for the anisotropy $v^2_{00}(z)$, derived from a given isotropic potential $v^0_{00}(z)$ according to Eqs. (2.5) and (2.6). Because of the smaller sensitivity of both the transition probabilities and RMSA resonance energies for HD to the form of $v^2_{00}(z)$, we shall use this as a check to differentiate between extremely different regions of the β_A, β_R parameter space but not to investigate small changes in the values of β_A β_R. This is an improvement on our earlier study of the HD/Ag(111) system[9] where for a much cruder model of $v^2_{00}(z)$, namely $\beta = \beta_A = \beta_R$, analysis of the RMSA resonance energies alone gave a preliminary order of magnitude estimate of β (representing an average of β_A and β_R).

C. Close coupled calculations

The close coupled equations to be solved are Eqs. (2.19) for $\mathbf{G} = \mathbf{0}$ and $m = 0$ (initial rotor state $|Jm\rangle = |00\rangle$). The total energy E is then replaced by E_{z_i}, the z component of the incident beam energy. For HD, $V_{00}(z,\theta)$ is replaced by $\tilde{V}_{00}(z,\theta)$, Eqs. (2.14)–(2.16). The use of the flat surface assumption to obtain the rotationally inelastic transition probabilities is justified for HD by the extremely small size of the diffraction relative to the rotational excitation, and for H_2 and D_2 by the absence of diffraction peaks for measurements made along the azimuth of weakest corrugation. To ensure an accurate comparison of resonance positions with the experimental data we replace the rigid rotor energies by the empirical rotor energies $E(J)$ (Table I). For HD at beam energies $E_b \sim 120$ meV we have only four open rotational channels. For H_2 and D_2, we have four and six open channels, respectively, which are reduced by symmetry to two open channels for H_2 scattering from initial state $J = 0$ and 3 open channels for D_2. The close coupled equations are solved with the variable step-variable interval size (VIVAS) integrator.[20] Typical running times are 6 s CPU time for a four channel system at $E_{z_i} = 60$ meV on a Vax 11/780 computer. The speed of this integrator is extremely useful for the multiple runs needed for an iterative search of the β_A, β_R parameter space even though the further time saving usually

TABLE I. Empirical rotor energies, $E(J)$,[a] for HD used in all close coupled scattering calculations. Rigid rotor energies are shown for comparison. The ground vibrational state of HD is assumed. All energies are in meV.

Rotor state J	Empirical $E(J)$	Rigid rotor energy
0	0.000	0.000
1	11.063	11.320
2	33.114	33.961
3	66.000	67.922
4	109.502	113.204
5	163.331	169.806

[a] H. W. Woolley, R. B. Scott, and F. G. Brickwedde, J. Res. Natl. Bur. Stand. **41**, 379 (1948).

available in multiple calculations at different energies is not possible when potential parameters are varied.

The best fit parameters for the VEP and exp-3 forms of $v_{00}^{0}(z)$, Eqs. (2.9) and (2.10) are given in Table II.[6,10]

The first order resonance shifts $\epsilon_{n,Jm}^{(1)}$ for H_2 and D_2 were evaluated directly from Eq. (2.23), using a Numerov–Cooley algorithm to evaluate the bound state eigenfunction with energy ϵ_n and then integrating over $v_{00,R}(z)$ and $v_{00,A}(z)$ [Eq. (2.8)] with a 6300 point Simpson's rule quadrature.

III. EXPERIMENTAL PROCEDURE

The experiments described in this paper were carried out in an ultra-high vacuum beam–surface scattering apparatus which has been previously described.[9,21] It consists of the following sections: a differentially pumped beam source manifold, a UHV crystal chamber which includes an Auger spectrometer and an ion sputtering gun, a doubly differentially pumped rotatable mass spectrometer, and a PDP-11 minicomputer which controls the experimental apparatus and collects the data through a CAMAC interface.

The p-H_2 and o-D_2, i.e., $J=0$ hydrogen, used in these studies were generated by passing either n-H_2 or n-D_2 through an in-line catalytic converter. This device essentially consists of a coaxial stainless steel tube assembly which contains a dispersed nickel catalyst in its outer section. During operation the converter is immersed in a liquid hydrogen Dewar. This induces the nuclear spin state distribution to relax to its equilibrium value at 20 K, i.e., 99.8% p-H_2 and 97.8% o-D_2. A detailed description of this converter has been previously presented in our earlier paper dealing with the hydrogen/Ag(111) isotropic potential.[10] The beam parameters used in this study were as follows: incident beam divergence 0.1°, $\Delta v/v = 4.5\%$ (H_2) and 6.5% (D_2).

TABLE II. Parameters for the isotropic component $v_{00}^{0}(z)$ of the laterally averaged interaction potential.

Potential	Parameters
Variable exponent	$D = 31.535$ meV $\lambda = 0.6335 a_0^{-1}$ $P = 4.2925$ $z_e = 2.3441 a_0$
Exponential-3	$D = 32.4616$ meV $\alpha = 1.2789 a_0^{-1}$ $z_e = 3.7572 a_0$

The HD used in these experiments was also generated catalytically by passing an 8:1 H_2:D_2 mixture through a stainless steel column which was packed with magnesium granules and heated to an operating temperature of 600 K. This 8:1 feed gas ratio was chosen in order to produce an HD beam of high intensity and narrow velocity spread ($\Delta v/v \approx 5\%$).[8,9,22] An in-line liquid nitrogen cooled molecular sieve trap was placed between the HD generator and the beam source in order to remove any trace moisture from the resulting 4:1 H_2:HD gas mixture. The HD after supersonic expansion is predominantly (>99%) in the $J=0$ state. This is implied from the absence of energy gain peaks, $J=1 \rightarrow 0$, in the experimentally observed angular distributions of HD scattering from the silver surface. (When the quality of the jet expansion is intentionally degraded by lowering the stagnation pressure $J=1 \rightarrow 0$ transitions can be clearly seen). The HD is typically expanded through a 20 μ nozzle at a pressure of 260 psi.

Three types of scattering data are reported in this paper: angular distributions which include rotationally inelastic peaks, time-of-flight distributions, and selective adsorption scans. The angular distributions were obtained by scanning the detector at 0.2° increments while holding the angle of incidence at a fixed value. During these measurements the incident beam was modulated with a 50% duty cycle chopper. This enabled two 32-bit scalers which were synchronized to the chopper to collect signal plus background and background only information. The appropriate subtractions were made after 6 s of counting at each 0.2° angular increment. Time-of-flight measurements were obtained with a 1% duty cycle dynamically balanced 8-slot chopper (0.020 in. wide slots, 6 in. diameter, typically running speed of 200–350 Hz) operating in conjunction with a 255 channel multichannel scaler (0.25 μs/channel dwell time). Selective adsorption data were collected by measuring the peak intensity of a given rotational and/or diffractive peak at incident angle increments of 0.2°. In practice, these data were collected by alternately moving the crystal polar angle by ~0.2° and then scanning the detector through the desired peak with the computer recording in real time both the intensity and corresponding incident and reflected polar angles. Peak heights determined in this manner include contributions from both the coherently scattered molecules and the diffuse inelastic background.

The Ag(111) crystal was cut from a 99.999% boule and initially polished at the Cornell Materials Preparation Laboratory. It was subsequently repolished, aligned with Laue x-ray backreflection, and mounted using procedures that were previously described in detail.[9] Crystal quality was confirmed by observing uniform and high He and H_2 reflectivities at several points along the surface of the crystal.

IV. H_2 AND D_2 ROTATIONALLY INELASTIC SCATTERING

A. Experimental results

In this section the experimentally determined rotationally inelastic $J=0 \rightarrow 2$ transition probabilities are present-

ed for both H_2 and D_2. The convention used for labeling the azimuthal angle ϕ is to assign $\phi = 0°$ to the $\langle 11\bar{2}\rangle$ direction and $\phi = 30°$ to $\langle 01\bar{1}\rangle$. The rotationally inelastic data presented in this section were taken at $\phi = 15°$ to avoid the overlaps that occasionally occur in the final angular distributions between weak diffraction peaks and weak $J = 0 \rightarrow 2$ transitions. This overlap of diffractive and inelastic transitions was most severe along $\phi = 0°$. As a check of our procedure, inelastic peaks that could be clearly measured at $\phi = 0°$ were fully analyzed, and found to be in agreement with the $\phi = 15°$ data within experimental uncertainty. The diffraction and simultaneous rotation-diffraction intensities will be discussed in a later publication.[11]

Figure 2 shows the angular distributions for n-H_2 scattering from Ag(111) at four incident polar angles which are separated sequentially by 5° angular increments. The $J = 0 \rightarrow 2$ peak is barely observable at $\theta_i = 40°$ and gradually emerges as a distinct peak in the shoulder of the $J = 0 \rightarrow 0$ specular peak as θ_i decreases towards the surface normal (i.e., the inelastic transition probability increases relative to the specular beam as E_{z_i} is systematically increased). The FWHM of the specular beam angular profiles shown in Fig. 2, $\sim 1.0°$, are just somewhat larger than that of the incident beam, $\sim 0.7°$, as expected for a high quality surface. The FWHM of the $J = 0 \rightarrow 2$ peaks are of course larger due to the kinematics of the scattering process—different velocities present in the incident beam velocity distribution are inelastically scattered into different outgoing angles.

Figure 3 shows the angular distributions for n-D_2 scattering from Ag(111) for a similar sequence of four incident polar angles (out of a total of six angles measured for n-D_2). The same trend of increasing inelastic transition probabilities as θ_i decreases towards normal incidence (E_{z_i} increasing) is again present. Also note that the inelastic peaks for D_2 are scaled up by a factor of 10 relative to the specular channel while those for H_2 are scaled by a factor of 100 even though the relative population of $J = 0$ in the incident beam is only about twice that for H_2. This implies that the relative inelastic transition probabilities of D_2 are significantly larger than those for H_2. This is to be expected from the much smaller rotational energy spacing of D_2 relative to H_2. The

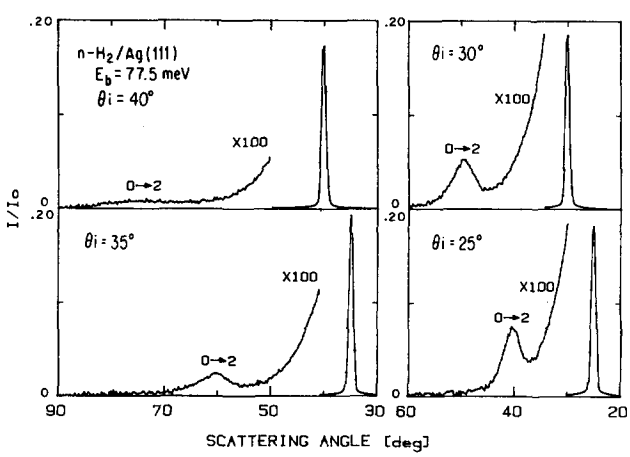

FIG. 2. Four angular distributions for n-H_2/Ag(111) with $\phi = 15°$ and $T_s = 125$ K.

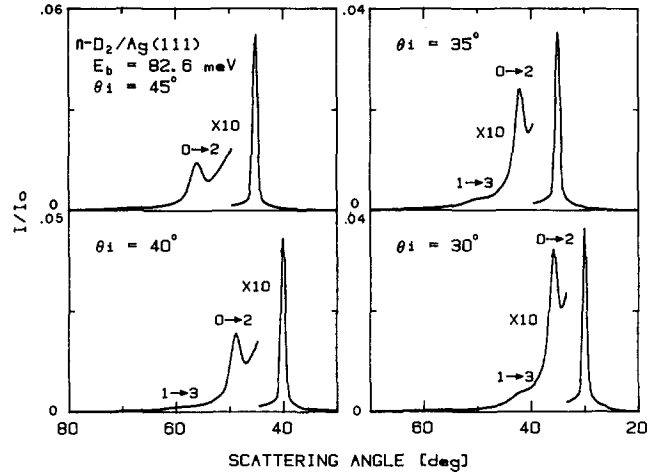

FIG. 3. Four angular distributions for n-D_2/Ag(111) with $\phi = 15°$ and $T_s = 125$ K.

$J = 1 \rightarrow 3$ transition is also energetically allowed for D_2, and is observed at several angles (Fig. 3).

B. Experimental analysis

The final scattering angles for nonresonant rotationally inelastic transitions are given by the following two kinematic constraints: (i) conservation of parallel momentum

$$\mathbf{K}_i = \mathbf{K}_f + \mathbf{G} \tag{3.1}$$

and (ii) conservation of total energy

$$k_i^2 = k_f^2 + \frac{2m}{\hbar^2}\left[E(J_f) - E(J_i)\right] \tag{3.2}$$

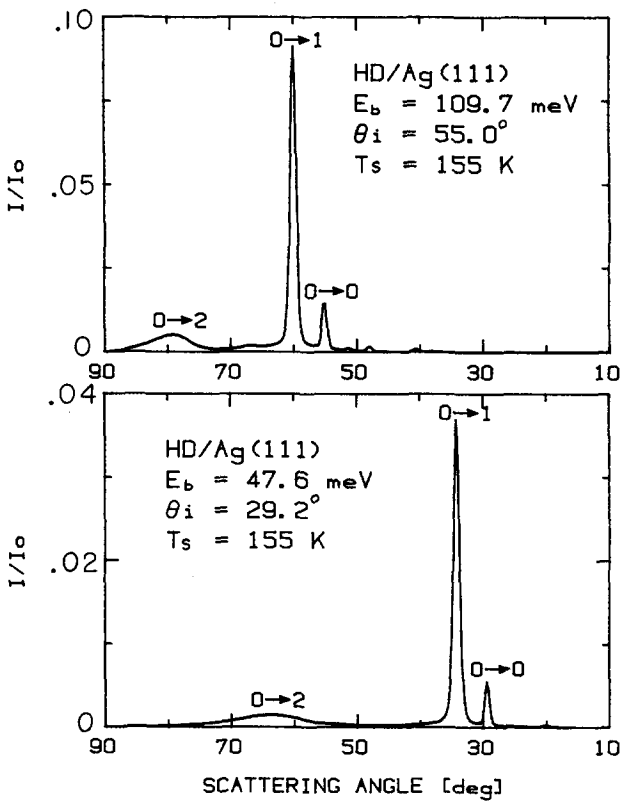

FIG. 4. Comparison of HD angular distributions taken at different beam energies but with the same E_{z_i}.

and are found to be in excellent agreement with the angles calculated using empirical rotor energies in Eq. (3.2) with $\mathbf{G} = \mathbf{0}$, i.e.,

$$k_{z_i}^2 = k_{z_f}^2 + \frac{2m}{\hbar^2}\,[E(J_f) - E(J_i)]. \tag{3.3}$$

This confirms that only the perpendicular component of the beam energy is involved in the energy transfer process. This is demonstrated in Fig. 4 which shows two HD angular distributions taken at the same E_{z_i} but using considerably different incident beam energies.

In order to directly compare the experimental results with transition probabilities obtained from quantum close coupled scattering calculations a detailed data reduction procedure was carried out. Experimental transition probabilities were obtained after (1) deconvoluting the instrumental contributions from the angular distributions, (2) correcting for Debye–Waller attenuation, and (3) accounting for the quantum statistics of the initial rotational state population distributions.

1. Deconvolution of final angular distributions

The supersonic molecular beam distribution is modeled by a standard shifted Gaussian:

$$p(v)dv = Nv^3 \exp[-(v - v_0)^2/\alpha^2]dv, \tag{3.4}$$

where v_0 is the stream velocity and α the Gaussian width. This can be readily transformed to the flight time distribution in terms of number density, which is the quantity directly determined by our detector. The measured time-of-flight data of the incident beam are predominantly a convolution of the true particle flight time distribution with the chopper gating function. This gating function was simulated by overlapping the beam's spatial diameter at the chopper (0.5 mm) with a moving chopper slit (width 0.51 mm). Convolution of an assumed flight time distribution with the gating function was fitted to the experimental distribution (after subtraction of the ion flight time in the detector) with a nonlinear least squares fittings routine to obtain the beam parameters.

Angular distributions were then fit with a simulation program based on the fitted incident beam characteristics, scattering kinematics, and the two-dimensional detector resolution function which was determined experimentally with the incident beam passing through a 0.05 mm aperature in the detector. This Gaussian-shaped function has an in-plane FWHM of 0.66° and out-of-plane FWHM of 0.40°. The diffuse background was modeled with a Gaussian function in terms of $(\theta_f - \theta_0)/\theta_w$ where θ_0 is the Gaussian origin and θ_w the width. These parameters were either assigned or freely fitted to get the best results. A nonlinear least squares fitting routine was used with the background model to fit the angular distribution data. The area of the coherent part of the peak (i.e., free of diffuse background) was then scaled to the area of the simulated peak derived from the incident beam parameters, scattering kinematics, and the detector function. Inelastic transition probabilities (still needing to be corrected for Debye–Waller attenuation and incident ensemble spin statistics) suitable for comparison with scattering calculations were obtained in this manner. A typical fit obtained with this procedure is shown in Fig. 5.

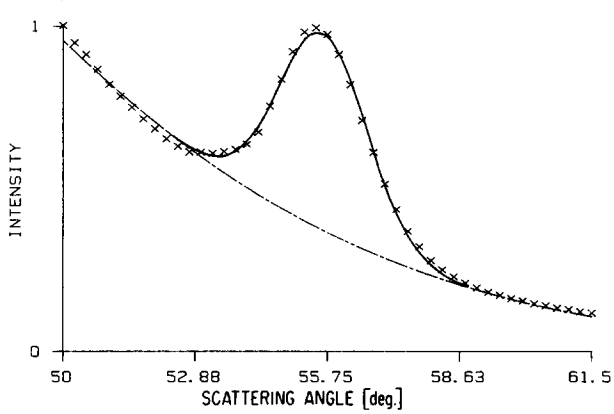

FIG. 5. Computer fit used to deconvolute the $J = 0 \rightarrow 2$ inelastic transition probability for D_2/Ag(111) at $\theta_i = 45°$. The solid line is the fit to the data (×) while the broken line is the fit to the diffuse background. The computer model clearly reproduces the experimental data very well.

2. Correction for thermal attenuation

The surface temperature dependence of the elastic scattering of H_2, D_2, and HD, and also the rotationally inelastic scattering of HD from Ag(111) has been analyzed in detail in a previous paper.[10] The Debye–Waller attenuation factor for a rotationally inelastic peak can be derived from the simplest treatment for atom–surface scattering:

$$\frac{I}{I_0} = \exp\left[\frac{-6m_g}{m_s k\theta_D}(E_i \cos^2\theta_i + D)T_s \times\left(1 + \sqrt{\frac{E_i \cos^2\theta_f + D}{E_i \cos^2\theta_i + D}}\right)^2\right], \tag{3.5}$$

where θ_i and θ_f are related by

$$E_i \cos^2\theta_f = E_i \cos^2\theta_i + \hbar^2[J_i(J_i + 1) - J_f(J_f + 1)]/2m_g. \tag{3.6}$$

Here m_g and m_s are the masses of the incident molecule and solid atoms, respectively, θ_D is the surface Debye temperature, and D the well depth of the laterally averaged interaction potential. The parameters θ_D and D extracted from temperature dependent studies are given in Table III, where it is apparent that a significant discrepancy is present between the homonuclear and heteronuclear results. Other evidence for the well depth discussed in our previous work on the isotropic potential component[10] indicates that the value of ~32 meV is the correct one. Since the applicability of standard Debye–Waller theory to molecule–surface collisions is not well established, the meaning of this difference between the isotopes is unclear. We therefore regard these parameters

TABLE III. Debye–Waller parameters for H_2 and D_2/Ag(111).

	E_i (meV)	D (meV)	θ_D (deg)
n-H_2	77.5	45.0	217
n-D_2	82.6	45.4	238
HD	109.7	31.9	228

TABLE IV. Incident beam rotational state populations for H_2 and D_2.

Gas	E_i (meV)	T_r (deg)	$J=0$	$J=1$	$J=2$	$J=3$
n-H_2	77.5	146	21.7	74.5	3.4	0.4
n-D_2	82.6	106	46.2	32.0	20.4	1.3
p-H_2	79.6	135	89.2	0.2	10.6	0.0

as an empirical means of correcting the experimental transition probabilities for thermal attenuation due to the motion of the target surface.

3. Initial rotational state distributions for H_2 and D_2

The rotational state distribution of the incident molecular beam can be calculated utilizing the energy balance equation[23]

$$\tfrac{5}{2}k_B T_0 + E_r(T_0) = \tfrac{1}{2}mv^2 + \tfrac{5}{2}k_B T_P + E_r(T_r), \qquad (3.7)$$

where T_0 is the nozzle temperature, T_P the parallel temperature of the beam, T_r the rotational temperature, m the molecular mass, v the terminal parallel velocity, and $E_r(T)$ the average rotational energy at temperature T. This energy balance equation, when combined with the assumption that the ortho and para spin components of the initial ensemble do not interconvert during supersonic expansion, allows the terminal rotational state distributions to be obtained. The results of this analysis are shown in Table IV for n-H_2, p-H_2, and n-D_2.

C. Experimentally derived inelastic transition probabilities

The rotationally elastic and inelastic transition probabilities for H_2 and D_2 are given in Tables V and VI, respectively. The $J=0\rightarrow 0$ transition probabilities were calculated by combining the specular intensity data from angular distribution measurements with the initial population distributions presented in Table IV. It was assumed that the elastic scattering probabilities for all of the initially populated rotational states were equal. This is a valid assumption for the hydrogen/Ag(111) system at the collision energies used in this study. As a final check of our data analysis procedure we also determined the $P(J=0\rightarrow 2)/P(J=0\rightarrow 0)$ ratios for H_2 and D_2 at selected collision energies using beams of pure p-H_2 and o-D_2. These ratios were found to be consistent within experimental error with the values obtained using n-H_2 and n-D_2. The $P(J=0\rightarrow 2)/P(J=0\rightarrow 0)$ ratios presented in Tables V and VI are the resulting relative transition probabilities.

TABLE V. Rotationally inelastic transition probabilities for n-H_2 and p-H_2. $T_s = 125$ K, $E_i = 77.5$ meV (n-H_2), $E_i = 79.6$ meV (p-H_2). Note that the experimental specular transition probabilities include several $J=n\rightarrow n$ components.

		Experimental		Debye–Waller corrected		
Gas	θ_i	Spec.	$0\rightarrow 2$	$0\rightarrow 0$	$0\rightarrow 2$	$(0\rightarrow 2)/(0\rightarrow 0)$
n-H_2	25	0.224	0.001 82	0.207	0.005 98	0.0289 ± 0.0043
	30	0.207	0.001 51	0.180	0.004 56	0.0254 ± 0.0038
	35	0.214	0.000 82	0.172	0.002 28	0.0133 ± 0.0027
	40	0.207	0.000 44	0.154	0.001 11	0.0072 ± 0.0014
p-H_2	27.5	0.210	0.005 10	0.448	0.010 25	0.0229 ± 0.0029

TABLE VI. Rotationally inelastic transition probabilities for n-D_2. $T_s = 125$ K, $E_i = 82.6$ meV. Note that the experimental specular transition probabilities include several $J=n\rightarrow n$ components.

	Experimental		Debye–Waller corrected		
θ_i	Spec.	$0\rightarrow 2$	$0\rightarrow 0$	$0\rightarrow 2$	$(0\rightarrow 2)/(0\rightarrow 0)$
25	0.0340	0.001 95	0.202	0.0203	0.1005 ± 0.0231
30	0.0447	0.002 14	0.234	0.0194	0.0829 ± 0.0149
35	0.0547	0.002 10	0.246	0.0164	0.0668 ± 0.0120
40	0.0650	0.001 84	0.253	0.0123	0.0486 ± 0.0063
45	0.0868	0.001 87	0.288	0.0106	0.0369 ± 0.0048
50	0.1102	0.001 78	0.311	0.0085	0.0274 ± 0.0036

D. H_2 and D_2 rotational transition probabilities: Comparison between experimental results and quantum scattering calculations

We now compare the experimental ratio of transition probabilities $P(J=0\rightarrow 2)/P(J=0\rightarrow 0)$ with the results of scattering calculations for both VEP and exp-3 based forms of the potential $V_{00}(z,\theta)$. Figure 6 shows the calculated ratio $P_c(J=0\rightarrow 2)/P_c(J=0\rightarrow 2)$ as a function of β_R for a range of values of β_A, at a constant normal incident energy $E_{z_i} = 53.2$ meV. The isotropic potential $v_{00}^0(z)$ and thus the basis for $v_{00}^2(z)$ here is the VEP. The experimental ratio is denoted by the solid horizontal line and the error bounds indicated by the dashed lines. The ratio $P_c(J=0\rightarrow 2)/P_c(J=0\rightarrow 0)$ shows a smooth variation as a function of β_A and of β_R: we note that for certain values of β_A there are two values of β_R giving the correct transition probability ratio. Repeating this search for each of the four normal incident

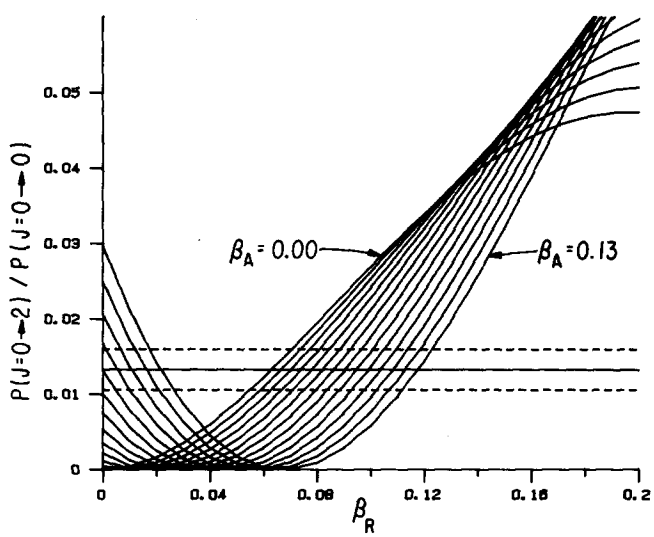

FIG. 6. Rotational transition probability ratio $P(J=0\rightarrow 2)/P(J=0\rightarrow 0)$ for H_2 measured as a function of β_R for a range of values of β_A, at incident energy $E_z = 53.2$ meV. Both parameters β_A and β_R are incremented by 0.01. The experimentally measured ratio is given by the solid horizontal line and the associated error bounds shown as dashed lines.

TABLE VII. Values of the repulsive anisotropic parameter β_R for β_A ranging from 0.00 to 0.20 calculated from the rotationally inelastic scattering of H_2 and D_2 with the variable exponent potential.[a]

	H_2 $E_b = 79.3$ meV				D_2 $E_b = 84.5$ meV					
θ_i:	40°	35°	30°	25°	50°	45°	40°	35°	30°	25°
E_z (meV):	46.5	53.2	59.5	65.1	34.9	42.3	49.6	56.7	63.4	69.4
β_A										
0.00	0.05	0.06	0.08	0.08	0.04	(0.045)	0.05	0.05	0.06	0.06
0.01	0.05	0.06	0.09	0.09	(0.045)	0.05	(0.055)	0.06	0.06	0.07
0.02	0.06	0.07	0.09	0.09	0.05	(0.055)	0.06	0.06	0.07	0.07
0.03	0.06	0.07	0.09	0.09	0.06	0.06	(0.065)	0.07	0.07	(0.075)
0.04	0.07	0.08	0.10	0.10	(0.065)	(0.065)	0.07	0.07	0.08	0.08
0.05	0.07	0.08	0.10	0.10	0.07	0.07	(0.075)	0.08	0.08	(0.085)
0.06	0.08	0.09	0.10	0.10	(0.075)	(0.075)	0.08	(0.085)	0.09	0.09
0.07	0.08	0.09	0.11	0.11	0.08	(0.085)	(0.085)	0.09	0.09	(0.095)
0.08	(0.085)	0.09	0.11	0.11	(0.085)	0.09	0.09	0.10	0.10	0.10
0.09	0.09	0.10	0.11	(0.115)	0.09	(0.095)	0.10	0.10	(0.105)	0.11
0.10	0.09	0.10	0.12	0.12	0.10	0.10	(0.105)	0.11	0.11	0.11
0.11	0.10	0.11	0.12	0.12	(0.105)	(0.105)	0.11	(0.115)	0.12	0.12
0.12	0.10	0.11	0.13	0.13	0.11	(0.115)	(0.115)	0.12	0.12	(0.125)
0.13	0.11	0.12	0.13	0.13	(0.115)	0.12	0.12	0.13	0.13	0.13
0.14	0.11	0.12	0.14	0.14	(0.125)	(0.125)	0.13	(0.125)	(0.135)	0.14
0.15	0.12	0.13	0.14	0.14	0.13	0.13	(0.135)	0.14	0.14	0.14
0.16	0.12	0.13	0.15	0.15	(0.135)	0.14	0.14	(0.145)	0.15	0.15
0.17	0.13	0.14	0.15	0.15	0.14	(0.145)	(0.145)	0.15	0.15	0.16
0.18	0.13	0.14	0.16	0.16	0.15	0.15	(0.155)	0.16	0.16	0.16
0.19	0.14	0.15	0.16	0.16	(0.155)	(0.155)	0.16	(0.165)	0.17	0.17
0.20	0.14	0.15	(0.165)	(0.165)	0.16	(0.165)	(0.165)	0.17	0.17	(0.175)

[a] The perpendicular energies $E_z = E_b \cos^2 \theta_i$ correspond to the experimental energies. These values of β_R were obtained by comparison of the calculated ratio of transition probabilities $P(J=0 \rightarrow 2)/P(J=0 \rightarrow 0)$ to the experimental ratios. Both β_A and β_R are incremented by 0.01 in this search. Interpolated values are given where appropriate and are bracketed to indicate this.

energies measured for H_2 and for the six normal incident energies for D_2 (Tables V and VI) produces at each normal incident energy E_{z_i} a whole set of parameter pairs β_A, β_R which will fit the H_2 or D_2 transition probability ratios, within the experimental error bounds. In Table VII we show the combinations β_A, β_R derived by scanning both β_A and β_R in increments of 0.01 for the VEP parametrization: the table contains the value of β_R for given β_A which brings the probability ratio $P(J=0 \rightarrow 2)/P(J=0 \rightarrow 0)$ closest to the experimental values for each energy. Although one or more values of β_R may fall between the experimental error bounds, for this grid spacing there are never two successive values, i.e., $\beta_R = \beta$ and $\beta_R = \beta + 0.01$ within these limits. Where successive values of β_R give ratios lying above and below the error bounds, an interpolated value of $\beta + 0.005$ has been used. For the values of β_A showing two possible values of β_R (e.g., $\beta_A = \pm 0.11$ in Fig. 7) simultaneous comparison at different energies allows one possibility to be eliminated because of an unrealistically sharp change in β_R with E_{z_i}. Table VII and the corresponding results for the exp-3 parametrization are summarized in Figs. 7 and 8. The crosses ($\times$) and ($+$) represent values of β_A, β_R which fit the experimental transition probability for H_2 and D_2, respectively, at any one of the above criterion. The circles in Fig. 8 represent combinations β_A, β_R derived from the n-H_2 shifts and linewidth broadening, to be discussed in Sec. V. Figures 7 and 8 thus show the combinations β_A, β_R which are most nearly energy (and isotope) independent. The finite width of the bands in β_A, β_R space does, however, imply that there is some residual energy and isotope dependence which is not accounted for by this parametrization of $v_{00}^2(z)$. The variation of these bands over the range of β_A, β_R shown here clearly demon-

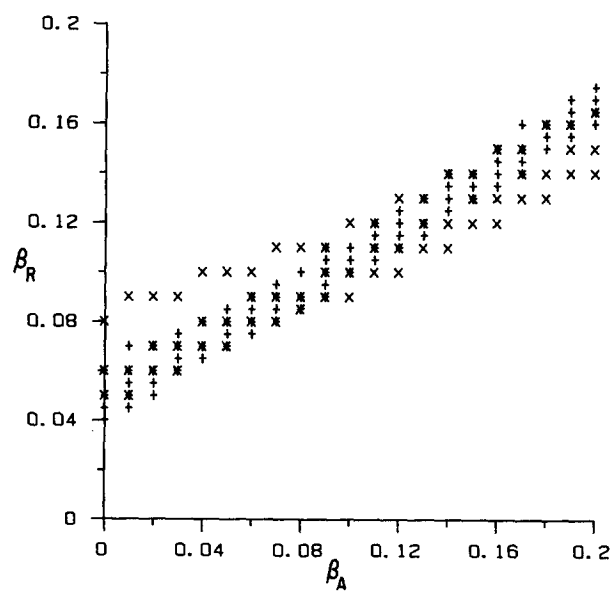

FIG. 7. Anisotropic parameter space β_A, β_R for the VEP potential showing the interaction between regions by fitting H_2 and D_2 rotationally inelastic transition probabilities. Crosses ($\times$) denote combinations derived from the H_2 rotationally inelastic transition probabilities, while pluses ($+$) are for D_2. The band of β_R values for given β_A reflects the energy dependence apparent in Table VII.

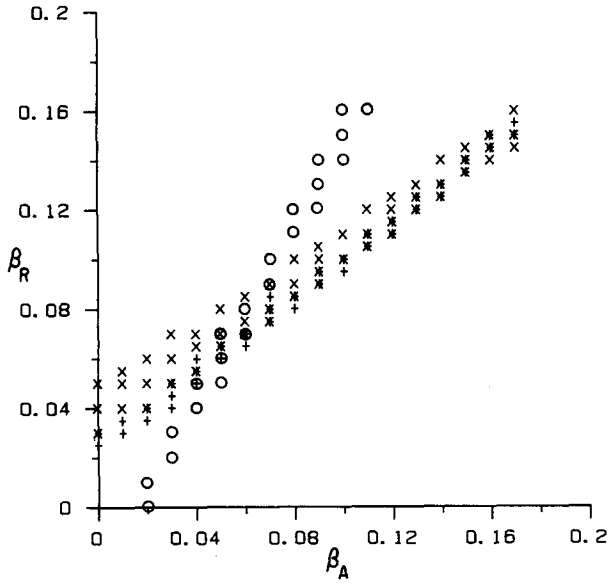

FIG. 8. Anisotropic parameter space β_A, β_R for the exp-3 potential showing the interaction between regions derived by fitting (i) H_2 and D_2 rotationally inelastic transition probabilities, and (ii) a single $|Jm\rangle$-averaged first order shift ΔE_n and linewidth broadening for n-H_2 adsorbed in the $n = 2$ level. Crosses (×) denote combinations derived from the H_2 rotationally inelastic transition probabilities while pluses (+) are for D_2. Circles (O) denote combinations derived from the n-H_2 shift and linewidth broadening in the $n = 2$ level (see Sec. V). The linewidth is measured as the FWHM of the n-H_2 distribution. Only distributions with one resultant peak or two peaks separated by less than 0.5 meV are included. Further selection is made by requiring the averaged shift ΔE to be in the range $+0.20 \pm 0.15$ meV and the linewidth to be in the range 0.35 ± 0.15 meV.

strate the coupled nature of the dependence of the two anisotropy parameters β_A and β_R. Slight differences apparent in the distribution over the β_A, β_R space between Fig. 7 and 8 are due to the weak variation of the potential anisotropy on the functional form of $v_{00}^0(z)$ as discussed in Sec. II [Eq. (2.8)].

Figure 9 shows the ratio $P_c(0 \to 2)/P_c(0 \to 0)$ as a function of incident energy E_{z_i} calculated for H_2 with $\beta_A = +0.06$[12] and three different values of β_R, for both VEP and exp-3 based potentials. The experimental ratios $P_c(J = 0 \to 2)/P(J = 0 \to 0)$ at the four incident energies of Table V are shown as crosses with associated error bars. Figure 10 is the corresponding plot of $P_c(0 \to 2)/P_c(0 \to 0)$ for D_2. For comparison we also include the results obtained for a single β parametrization, as used in our early work[9] with $\beta = \beta_A = \beta_R = +0.10$. These curves are very close to the curves obtained with $\beta = -0.10$, as expected for weakly inelastic scattering first order in the strength of the anisotropic potential component. The H_2 results typically show threshold resonances. It is apparent from each of these figures that no single combination β_A, β_R manages to fit the rotational transition probability ratios exactly, at all energies and for both isotopes. However, this empirical fitting procedure does manage to distinguish between very different regions of the parameter space β_A, β_R. This is shown in Fig. 11 where the ratio $P_c(0 \to 2)/P_c(0 \to 0)$ is plotted as a function of E_{z_i} for both VEP and exp-3 based potentials with $\beta_A = +0.05, \beta_R = +0.20$, and compared with the (i) VEP based potential, $\beta_A = +0.06, \beta_R = +0.09$ and (ii) the exp-3 based potential, $\beta_A = +0.06, \beta_R = +0.08$. The values $\beta_A = +0.05, \beta_R = +0.20$ are those derived by Schinke *et al.* on the basis of the magnitude of magnetic sublevel splittings for $J = 1$ H_2 DSA resonances on the Ag(110) surface[7,19] assuming a VEP based parametrization of the same form as Eq. (2.8) with nearly identical isotropic potential param-

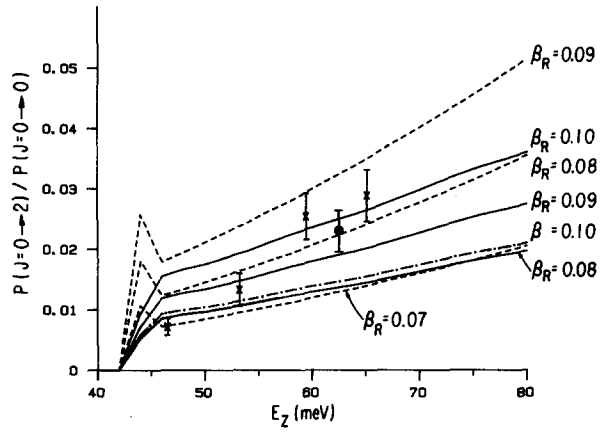

FIG. 9. Rotational transition probability ratio $P(J = 0 \to 2)/P(J = 0 \to 0)$ for H_2 as a function of E_z, calculated for different forms of $v_{00}^0(z)$ and $v_{00}^2(z)$. Results from the VEP based potential equation (2.9) with $\beta_A = +0.06$, $\beta_R = +0.08$, $+0.09$, $+0.10$ are shown as solid lines (—). Results for the exponential-3 based potential, Eq. (2.10) with $\beta_A = +0.06, \beta_R = +0.07$, $+0.08$, $+0.09$ are shown as dashed lines (---). Results for the VEP based potential with the single β anisotropy $\beta = \beta_A = \beta_R = +0.10$ are shown as dot–dashed lines (– · – · –). Calculations were performed at increments of 2.0 meV in E_z. Experimental values are denoted by crosses (×) and associated error bars. The data point denoted by a dot (•) was determined using a p-H_2 incident beam.

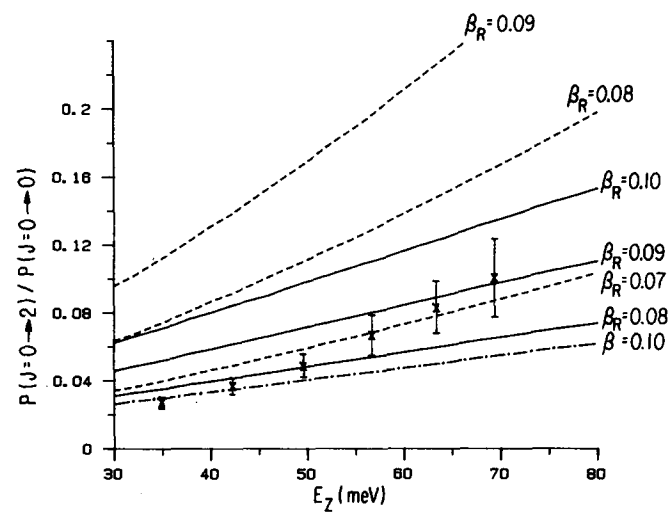

FIG. 10. Rotational transition probability ratio $P(J = 0 \to 2)/P(J = 0 \to 0)$ for D_2 as a function of E_z, calculated for different forms of $v_{00}^0(z)$ and $v_{00}^2(z)$. Results from the VEP based potential equation (2.9) with $\beta_A = +0.06, \beta_R = +0.08$, $+0.09$, $+0.10$ are shown as solid lines (—). Results for the exponential-3 based potential, Eq. (2.10) with $\beta_A = +0.06$, $\beta_R = +0.07$, $+0.08$, $+0.09$ are shown as dashed lines (---). Results for the VEP based potential with the single anisotropy $\beta = \beta_A = \beta_R = +0.10$ are shown as dot–dashed lines (– · – · –). Calculations were performed at increments of 2.0 meV in E_z. Experimental values are denoted by crosses (×) and associated error bars.

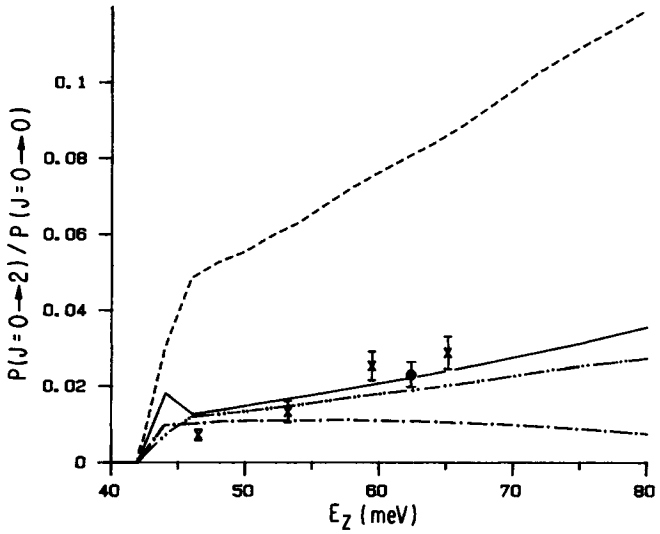

FIG. 11. Rotational transition probability ratio $P(J=0\rightarrow 2)/P(J=0\rightarrow 0)$ for H_2 as a function of E_z showing the effects of large variations in the parametrization of $v_{00}^2(z)$. The solid line (—) is the result of the exponential-3 based potential with parameters of Table II and anisotropy $\beta_A = +0.06, \beta_R = +0.08$ while the (- · - ·) line is the result for the exponential-3 potential with anisotropy $\beta_A = +0.05, \beta_R = +0.20$. The (- · · - · ·) line is the result for the VEP based potential with parameters of Table II and anisotropy $\beta_A = +0.06, \beta_R = +0.09$, while the dashed line (---) is the result for the VEP potential with anisotropy $\beta_A = +0.05, \beta_R = +0.20$. Calculations were performed at increments of 2.0 meV. Experiment values are donated by crosses (×) for n-H_2 derived values and a dot (•) for the p-H_2 derived value.

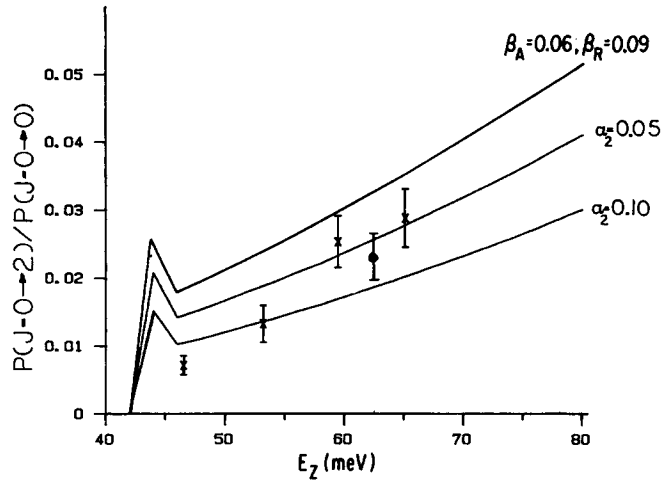

FIG. 12. Rotational transition probability ratios $P(J=0\rightarrow 2)/P(J=0\rightarrow 0)$ for H_2 as a function of E_z for the exponential-3 based potential with the three parameter anisotropic term given by Eq. (2.12). Results are shown for anisotropy parameters $\beta_A = +0.06$, $\beta_R = +0.09$, with $\alpha_2 = +0.05$, $+0.10$ (—). The isotropic parameters are given in Table II. Calculations are carried out on a grid of 2.0 meV in E_z. Experimental values are denoted by crosses (×) and associated error bars. The data point denoted by a dot (•) was determined using a p-H_2 incident beam.

eters.[7] It is clear from Fig. 11 that the anisotropy $\beta_A = +0.05, \beta_R = +0.20$ gives unacceptable values for the homonuclear rotational transition probability ratio. Furthermore, whereas for $\beta_A = +0.06, \beta_R \sim 0.08$–$0.09$ the ratio $P_c(0\rightarrow 2)/P_c(0\rightarrow 0)$ is very similar for both exp-3 and VEP based potentials, when the parameters β_A and β_R are significantly different, such as, e.g., $\beta_A = +0.05$, $\beta_R = +0.20$, there is a marked difference between the energy dependence of the rotational transition probability ratio for the two different pairs of functional forms of $v_{00,R}(z)$ and $v_{00,A}(z)$. Thus one has to be very careful in substantiating the anisotropy parameters β_A, β_R obtained from a fit to a given experimental quantity. When $\beta_A \sim \beta_R$ the form of $v_{00}^2(z)$ is insensitive to the functional form of two numerically similar potentials $v_{00}^0(z)$ (Fig. 21 of Ref. 10). However, when β_A and β_R differ by a large factor, the form of $v_{00}^2(z)$ becomes sensitive to the functional forms of $v_{00,R}(z)$ and $v_{00,A}(z)$ and hence, in a general sense to $v_{00}^0(z)$.

When the three parameter form of $v_{00}^2(z)$ was used, e.g., Eq. (2.12), a slight improvement over the results of Figs. 9 and 10 was found. Figure 12 shows the rotational transition probability ratios for H_2 calculated with the exp-3 based potential with $\beta_A = +0.06$, $\beta_R = +0.09$ and $\alpha_2 = 0.0$, $+0.05$, $+0.10$. The three parameter curves show more pronounced curvature and thus qualitatively show increased resemblance to the experimental results. Note, however, that no single parametrization was found that could fit the experimental ratios for both homonuclear isotopes at all collision energies.

To summarize the results of this section, we find that a comparison between experimental and calculated rotational transition probability ratios for the weakly inelastic H_2 and D_2 scattering over a range of incident energies E_{z_i} imply a range of possible combinations β_A, β_R for a given $v_{00}^0(z)$. In order to isolate a single pair of values, it is necessary to consider additional, independent experimental information. Both the VEP and exp-3 based forms of $V_{00}(z,\theta)$ with the parametrization of Eq. (2.8) give similar bands of acceptable β_A, β_R combinations, each of which accounts for all the experimentally measured transition probability ratios to a first approximation. However, the finite width of these bands implies some residual energy dependence which is not accounted for by either potential with a two parameter anisotropic term. This energy dependence is partially reduced by the modification of the repulsive term in $v_{00}^2(z)$ to include an additional softness parameter.

V. BOUND LEVEL RESONANCES AND LINE SHAPE ANALYSIS FOR n-H_2 AND p-H_2

In this section the DSA resonance energies for p-H_2 and n-H_2 are analyzed in order to derive information on the spatial anisotropy of $V_{00}(z,\theta)$ which is complementary to that obtained via rotational inelastic scattering. This analysis is based on the fact that the DSA bound level resonances for n-H_2 actually consist of multiplets, with this substructure arising from the J and m dependence of the resonance energies, $E_n = \epsilon_n + \epsilon_{n,Jm}^{(1)}$. This point was fully discussed in Sec. II B, with specific reference being made to Eqs. (2.22)–(2.24).

Unfortunately, distinct splittings have not been observed in our DSA data for either n-H_2 or n-D_2 on Ag(111).[6,10] This can be attributed to the finite energy resolution and sensitivity limitations of our instrument, and, more importantly, to the *extremely* weak diffractively coupled re-

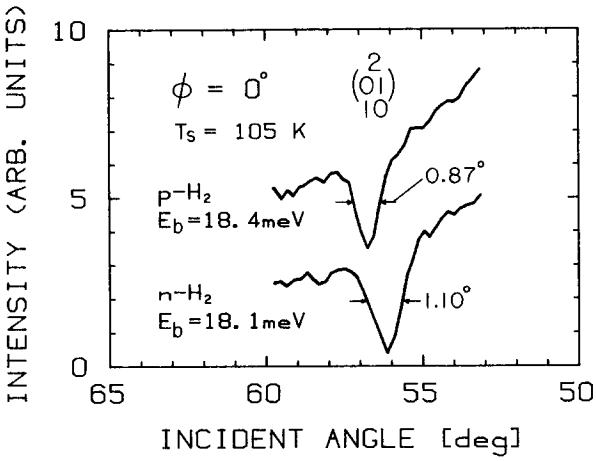

FIG. 13. Selective adsorption linewidth broadening for n-H_2 relative to p-H_2. The total shift in dip angle is due to both small $|J,m\rangle$-dependent level shifts for n-H_2 and the difference in beam energies.

sonances which are observed on Ag(111), a closest packed metallic surface. However, for the $n = 2\binom{10}{01}$ resonance along the $\langle 11\bar{2}\rangle$ direction we have observed a distinct and reproducible example of resonance line shape broadening for n-H_2 relative to p-H_2, as shown in Fig. 13. The deconvoluted FWHM energy widths of these resonances are 0.19 ± 0.04 meV for p-H_2 and 0.35 ± 0.01 meV for n-H_2. These values represent the averages obtained from three independent measurements for each resonance, with the p-H_2 and n-H_2 data taken sequentially for each of the three different data sets in order to optimize the precision of the relative line shape determinations. The average deconvoluted resonance linewidths resulting from these measurements are 0.47° for p-H_2 and 0.86° for n-H_2. This broadening arises from the superposition of the DSA resonances for the $|J,m\rangle = |0,0\rangle$, $|1,0\rangle$, and $|1,\pm 1\rangle$ substates present in $n = H_2$, weighted respectively as $\frac{1}{4}:\frac{1}{4}:\frac{1}{2}$.

The $n = 2$ data for n-H_2 can be used to obtain quantitative information on $v_{00}^2(z)$ by carrying out an accurate computer simulation of the broadened line shape. Such a computer program, which includes a full convolution over the experimental parameters, has been constructed. It requires as input the DSA resonance energies for each $|J,m\rangle$ state, which can be calculated using Eqs. (2.23) and (2.8). It also requires as input the linewidth for each component of the multiplet. These were obtained by assuming that the linewidth of each $|J,m\rangle$ sublevel in a given bound state, n, is the same as that for p-H_2 in that state, i.e., for the $|0,0\rangle$ resonance. This line shape program has been used to examine (i) for what range of anisotropy parameters β_A and β_R a single broad resonance is produced and (ii) which anisotropy parameters to give a resultant line shape of 0.35 meV for n-H_2, with its minimum shifted by ~ 0.20 meV from that for $|0,0\rangle$. (Note that although the center-of-gravity of the n-H_2 multiplet is unchanged relative to the DSA resonance for p-H_2, the line shape can be skewed since the $|1,\pm 1\rangle$ peak is weighted twice that of the $|1,0\rangle$ resonance.)

The type of analysis outlined above should ideally be carried out for each bound level of $v_{00}^0(z)$, for both n-H_2 and n-D_2. However, as was mentioned above, detailed experimental information is only available for the $n = 2$ level of H_2. We shall therefore restrict our attention to this level. Nevertheless, it is worth mentioning that the compilation of DSA data for p-H_2, n-H_2, o-D_2, and n-D_2 presented in Refs. 6 and 10 exhibits two general trends: The DSA shifts between p-H_2 and n-H_2 are larger than those between o-D_2 and n-D_2, and the shifts of both isotopes decrease as the bound level quantum number, n, increases. The first part reflects the different weighting of the $|J,m\rangle$ states in n-H_2 and n-D_2, and the linewidths of the individual adsorbed $|J,m\rangle$ resonance states. The second feature is primarily a consequence of the decrease in expectation value $\langle n|v_{00}^2(z)|n\rangle$ as n increases.

The experimental line shapes of the p-H_2 and n-H_2 resonance dips were analyzed in two steps. First, the deconvoluted Lorentzian linewidth of the p-H_2 dip was obtained by fitting the experimental line shape with a forward convolution program. This program initially folds an assumed DSA Lorentzian line shape with the incident beam's velocity distribution to obtain a broadened resonance line shape in terms of resonance energy. It then transforms this line shape into a function of incident angle, and folds this with the detector resolution function. Forward convolutions of this type were then carried out by systematically varying Γ, the HWHM of the input Lorentzian line shape, until the simulated resonance came into good agreement with the experimental $n = 2$ p-H_2 data. This comparison was facilitated by first fitting the experimental resonance line shape to a Gaussian function after subtracting the appropriate background. The upper panel of Fig. 14 demonstrates that the experimen-

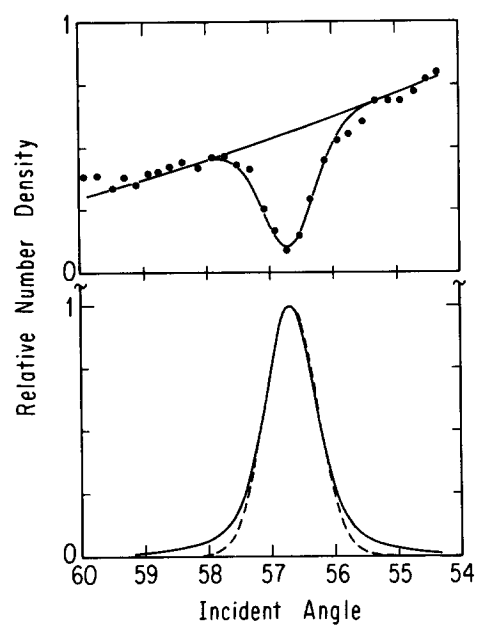

FIG. 14. Selective adsorption resonance line shape for the $n = 2$ level of the p-H_2/Ag(111) physisorption potential. The upper panel shows the best Gaussian fit (solid line) to the data (•) including the sloping background (see Fig. 15). The lower panel contains the same Gaussian fit to the data as above but without background (---) and the *simulated* line shape (—). The computer simulation is a full convolution of a Lorentzian line shape (HWHM 0.05 meV) with the detector resolution function and the velocity spread of the incident beam.

tal p-H_2 resonance is well described by this procedure, i.e., by a Gaussian line shape with a broadly sloping quadratic background. The lower panel of this figure shows the best fit simulation of this DSA resonance (solid line), which occurs for $\Gamma = 0.05$ meV. Simulations using $\Gamma = 0.5$ meV and $\Gamma = 0.005$ meV produce qualitatively poorer fits than that shown in Fig. 16. $\Gamma = 0.05$ meV is used as the linewidth for each of the multiplet components in the n-H_2 simulation discussed below.

In the second step of the analysis simulated n-H_2 line shapes were constructed by superimposing the resonances for $|J,m\rangle = |0,0\rangle$, $|1,0\rangle$, and $|1,\pm 1\rangle$ using resonance energies calculated for a variety of anisotropy parameters β_A, β_R. These multiplet energies were calculated using Eqs. (2.23) and (2.8). The angular integrals used in evaluating these shifts were $\langle 00|P_2|00\rangle = 0$, $\langle 10|P_2|10\rangle = +0.4$, and $\langle 1,\pm 1|P_2|1\pm 1\rangle = -0.2$. The expectation values $\langle n|v_{00}^2(z)|n\rangle$ were evaluated for both the exp-3 and VEP parametrizations of $v_{00}^0(z)$, Eqs. (2.9)–(2.11).

Figure 15 displays the simulated line shapes for five sets of β_A, β_R, while in Fig. 16 those for three extreme sets of β_A, β_R are shown along with the experimental line shape. The exp-3 potential was used for all of the simulations in Fig. 15 and 16. Examination of these two figures reveals that the data are most clearly reproduced by simulations employing $\beta_A \sim 0.06$, with β_R falling between 0.09 and 0.11. The lower panel of Fig. 16 suggests that the value of β_R proposed by Schinke, 0.20, is too large,[19] as a clearly resolved triplet is predicted, in contradiction to the experimental observation of a single (broadened) peak.

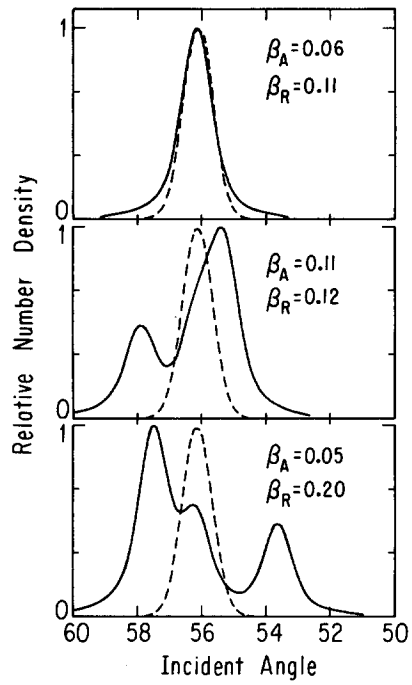

FIG. 16. Three additional simulations of the $n = 2$ resonance at $\phi = 0°$ (see Fig. 15) for a wide parameter sampling. Dashed curves: experimental line shape; solid lines: computer simulations including the instrument transfer function.

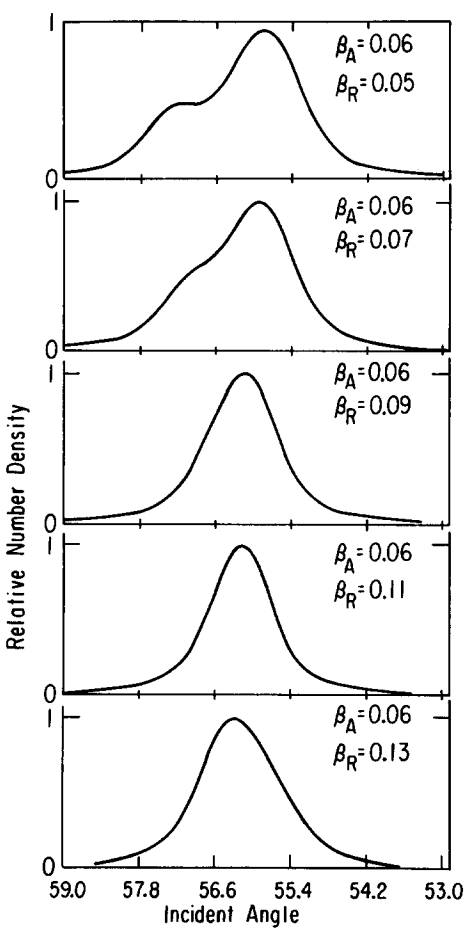

FIG. 15. n-H_2 selective adsorption line shape simulations for the $n = 2$ resonance shown in Fig. 15 as a function of β_A, β_R. Input: $\Gamma = 0.05$ meV, beam velocity spread 0.09 meV, detector resolution 0.66°.

The results of the full β_A, β_R parameter are shown as open circles in Fig. 8. These circles denote calculated line shapes having energy shifts ΔE in the range 0.20 ± 0.15 meV with respect to p-H_2, and linewidths in the range 0.35 ± 0.15 meV. It is interesting to see that these circles intersect the rotationally inelastic scattering data which is also displayed in Fig. 7 at $\beta_A \sim 0.06$—the value calculated by Harris and Feibelman,[12] and $\beta_R \sim 0.08$—the value calculated by Harris and Liebsch for H_2/Cu(100),[13] but smaller than the β_R value of Nordlander and Holmberg, 0.18.[24]

For completeness, we end this section by reporting our calculated shifts for the $|J,m\rangle = |1,0\rangle$ level (with respect to $|0,0\rangle$) for all of the bound levels of H_2/Ag(111) using both the exponential-3 and VEP parametrizations of $v_{00}^0(z)$. These shifts, for two different sets of β_A and β_R, are shown in Table VIII. The shifts of the $|J,m\rangle = |1,\pm 1\rangle$ levels can be easily derived from Table VIII by remembering that $\Delta\epsilon_{n,1\pm 1} = -(\Delta\epsilon_{n,10})/2$. The results shown in this table serve to emphasize that the level shifts calculated with Eq. (2.23) depend not only on the values of β_A and β_R employed in Eq. (2.8), but also on the parametric form of $v_{00}^0(z)$, the laterally averaged isotropic potential.

VI. HD ROTATIONAL TRANSITION PROBABILITIES AND RESONANCES

A. Experimental results

In this section the experimentally determined rotationally inelastic transition probabilities for HD are presented.

TABLE VIII. Calculated energy level shifts $\Delta\epsilon_n$ for $J = 1, m = 0$ hydrogen adsorbed on Ag(111) for the exponential-3 and variable exponent parametrizations of $v_{00}^0(z)$.[a]

$v_{00}^0(z)$:	Exponential-3		Variable exponent	
β_A/β_R:	0.06/0.09	0.05/0.20	0.06/0.09	0.05/0.20
Bound level n	$\Delta\epsilon_n$	$\Delta\epsilon_n$	$\Delta\epsilon_n$	$\Delta\epsilon_n$
0	−0.215	1.747	−0.356	1.068
1	−0.175	1.377	−0.303	0.738
2	−0.139	0.995	−0.241	0.485
3	−0.105	0.642	−0.177	0.298
4	−0.072	0.362	−0.117	0.166
5	−0.043	0.176	−0.067	0.081

[a] $\Delta\epsilon_n$ is defined here as $\Delta\epsilon_n = \epsilon_{n,10}^{(1)} - \epsilon_{n,00}^{(1)}$, and is presented in units of meV.

These angular distributions were taken at incident angle increments of 5°, spanning the range from $\theta_i = 25°$ to $\theta_i = 85°$, for two beam energies. Figure 17 shows a typical angular distribution and the corresponding Ewald representation of the scattering kinematics. All of the diffractive and rotationally inelastic peaks, labeled as $J_i \rightarrow J_f$ in this figure, are directly interpretable in terms of (i) parallel momentum conservation, Eq. (3.1), and (ii) conservation of total energy, Eq. (3.2). A full discussion of the scattering kinematics for HD/Ag(111) has been previously presented,[9] and will not be repeated here. The main features of the HD/Ag(111) system are the extremely high rotationally inelastic transition probabilities for HD relative to H_2 and D_2 (see Figs. 2, 3, and 17), and the presence on only weak diffraction for $\mathbf{G} \neq 0$. The first observation can be attributed to the offset of the HD center-of-mass from its geometric center, while the second indicates that the HD/Ag(111) potential has very low corrugation. This latter point was discussed in Sec. IV and allows us to treat Ag(111) to first approximation as a flat surface in the scattering calculations presented in this paper. Similar observations have also been recently reported for HD/Pt(111).[22] It is apparent from Figs. 4 and 17 that $J = 1$ or higher rotational states are nearly absent in the incident beam, as evidenced by the small $\Delta J = 1 \rightarrow 2$ peaks in these figures. We shall therefore treat the incident HD$|J,m\rangle$ ensemble as consisting exclusively of the $|0,0\rangle$ state in our data analysis and theoretical calculations. Finally, our rotational assignments (made initially on the basis scattering kinematics) have been independently confirmed by recording the actual time-of-flight distributions of the scattered molecules, as shown in Fig. 18 for $\theta_i = 25°$. These four velocity distributions are in excellent agreement with those predicted by the conservation of parallel momentum and total energy.

Six HD angular distributions, taken at incident angle increments of 10°, are shown in Fig. 19. These distributions

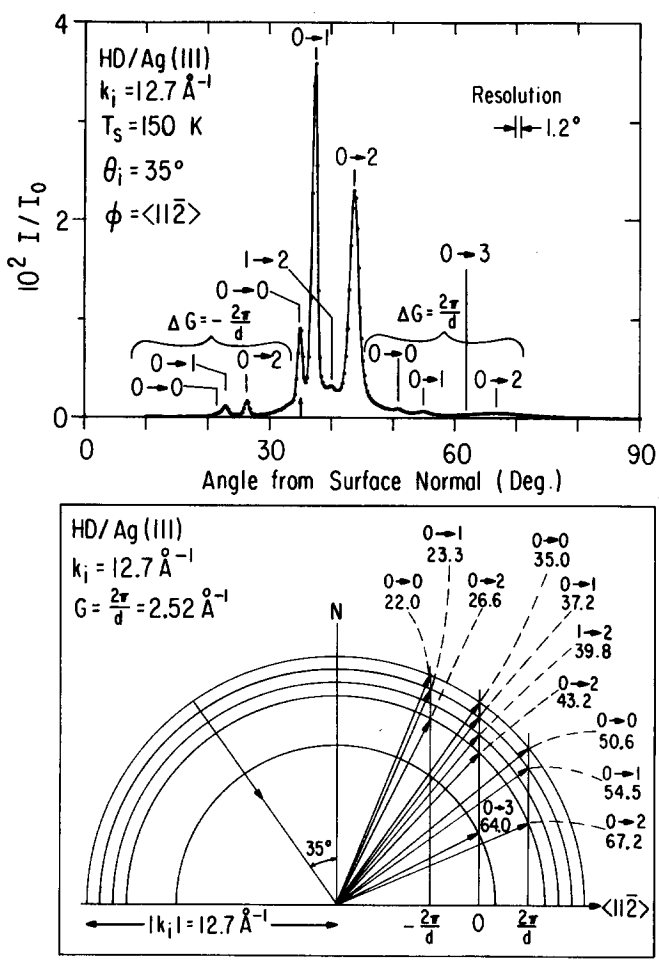

FIG. 17. Angular distribution of the reflected number density for HD scattering from Ag(111) along the ⟨11$\bar{2}$⟩ direction. Rotationally inelastic transitions are labeled $J_i \rightarrow J_f$. Vertical lines denote the predicted peak locations for a monoenergetic beam with $k_i = 12.7$ Å^{-1}. The lower section is an Ewald representation of the displayed angular distribution.

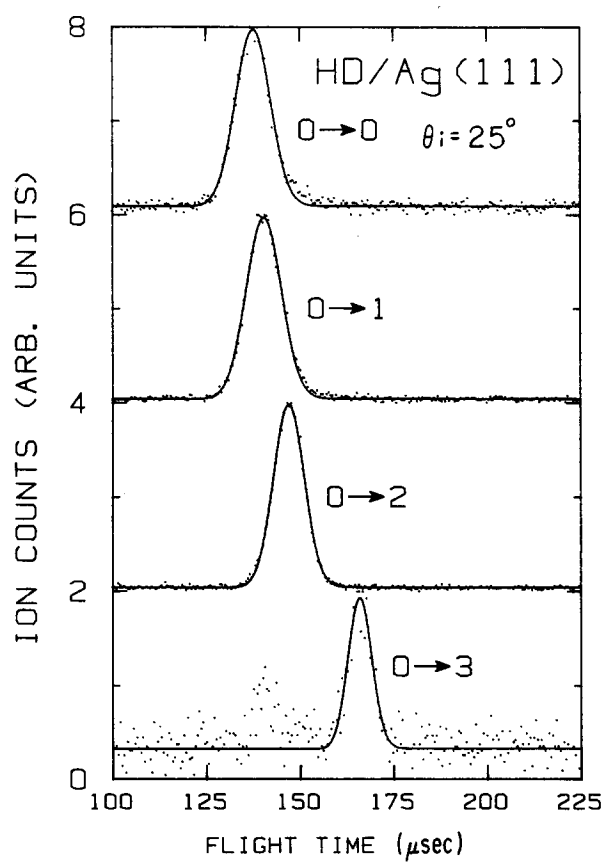

FIG. 18. HD time-of-flight distributions taken at the peak positions of the various elastic and rotationally inelastic channels.

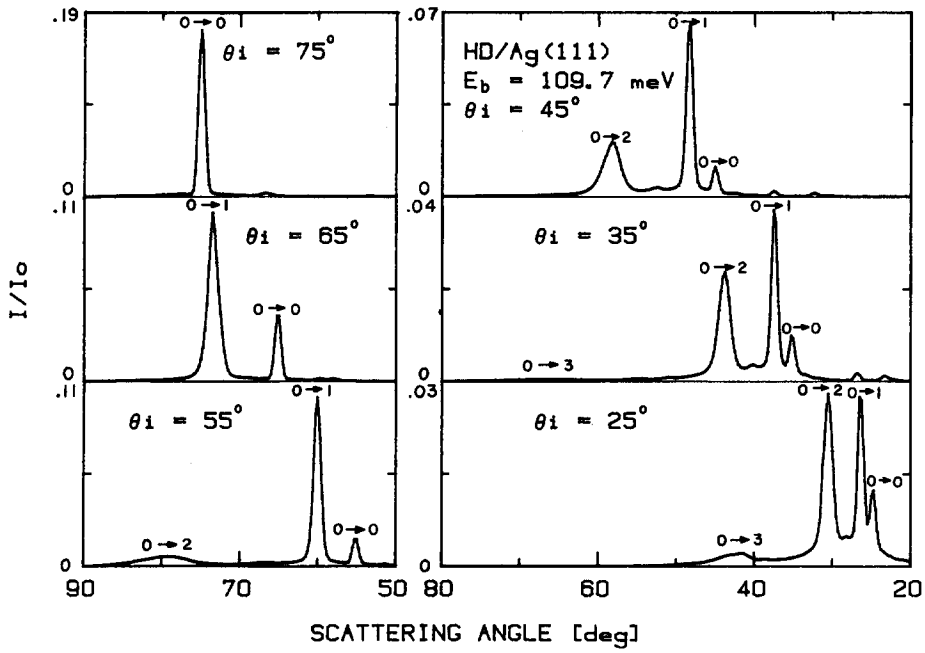

FIG. 19. Angular distributions of the reflected number density for HD/Ag(111) taken at six incident angles. Rotationally inelastic transitions are labeled $J_i \rightarrow J_f$. Note that higher inelastic channels appear whenever the normal component of the incident beam energy exceeds the rotational transition energy.

demonstrate that additional inelastic channels become accessible as θ_i decreases towards the surface normal, i.e., as the normal component of the incident beam energy increases. The deconvoluted inelastic transition probabilities for the room temperature and cryogenically cooled HD beams are given in Tables IX and X, respectively. These results were derived from the experimental angular distributions using the same procedures as were used in Sec. IV for treating H_2 and D_2. The theoretical calculations presented in the next section were compared to the Debye–Waller corrected data listed in Table IX after rescaling the transition probabilities such that they sum to unity for each angular distribution. This normalization procedure ignores the peaks associated with $\mathbf{G} \neq 0$, which account for less than 5% of the reflected flux. Our data analysis and normalization procedures were checked by comparing the transition probabilities derived from Tables IX and X as a function of E_{z_i}. These energy dependent final state distributions (for two different beam energies) were found to be superimposable—validating our analysis procedures, and again confirming that the flat surface approximation is valid for the HD/Ag(111) system.

B. Theoretical analysis

In this section we compare the theoretical predictions for the HD rotational transition probabilities and RMSA resonances with the experimental results, using the anisotropy parameters that were derived in Secs. IV and V from the H_2 and D_2 results. As discussed earlier in Sec. II, both the rotationally inelastic scattering and resonance energies for HD are relatively insensitive to small changes in the anisotropy of the potential, $v_{00}^2(z)$, and we include these results here primarily for confirmation of the conclusions from H_2 and D_2, to differentiate between widely separated areas of the β_A, β_R parameter space, and for completeness. We note that

TABLE IX. Rotationally inelastic transition probabilities for HD/Ag(111). $T_s = 155$ K, $E_i = 109.7$ meV.

	Experimental				Debye–Waller corrected			
θ_i	$0 \rightarrow 0$	$0 \rightarrow 1$	$0 \rightarrow 2$	$0 \rightarrow 3$	$0 \rightarrow 0$	$0 \rightarrow 1$	$0 \rightarrow 2$	$0 \rightarrow 3$
25	0.0115	0.0326	0.0455	0.00665	0.217	0.539	0.571	0.054
30	0.0097	0.0412	0.0471	0.00440	0.152	0.563	0.483	0.054
35	0.0104	0.0487	0.0512	0.00289	0.131	0.539	0.430	0.015
40	0.0104	0.0649	0.0593	...	0.105	0.574	0.397	...
45	0.0118	0.0925	0.0614	...	0.095	0.649	0.325	...
50	0.0142	0.1217	0.0651	...	0.090	0.678	0.273	...
55	0.0212	0.1638	0.0509	...	0.108	0.729	0.170	...
60	0.0338	0.2186	...	...	0.139	0.789	...	...
65	0.0546	0.2235	...	...	0.186	0.666	...	...
70	0.0737	0.2121	...	...	0.214	0.537	...	...
75	0.2472	...	...	...	0.691[a]	...	...	...
80	0.2405	...	...	...	0.774[a]	...	...	...
85	0.2062	...	...	...	0.846[a]	...	...	...

[a] Corrected for the geometrical loss of incident beam flux which occurs for $\theta_i \gtrsim 75°$.

TABLE X. Rotationally inelastic transition probabilities for HD/Ag(111). $T_s = 155$ K, $E_i = 47.6$ meV.

	Experimental			Debye–Waller corrected		
θ_i	$0 \to 0$	$0 \to 1$	$0 \to 2$	$0 \to 0$	$0 \to 1$	$0 \to 2$
29.2	0.0066	0.0546	0.0147	0.0337	0.244	0.0492
40.5	0.2830	0.0125	0.0788	0.0516	0.285	...
58.6	0.0352	0.1009	...	0.1020	0.255	...
74.7	0.1186	...	...	0.2730	...	...

since the isotropic potential was determined by the DSA resonances of H_2 and D_2 for $J = 0$, its determination is independent of the values of β_A and β_R assumed. Therefore no iteration of the isotropic and anisotropic potentials is required.

The calculated rotational transition probabilities $P_c(0 \to J')$, $J' = 0,1,2,3$ are shown in Figs. 20 and 21 as a function of E_{z_i}, for the VEP based potential with $\beta_A = 0.06$, $\beta_R = +0.09$ and for the exponential-3 based potential with $\beta_A = +0.06, \beta_R = +0.08$, respectively. The experimental values (unitarized transition probabilities from Table IX) are shown as crosses in these figures. The results from these two potentials are very similar, and are in good agreement with the experimental results. Although the HD transition probabilities show little sensitivity to *small* changes in the anisotropy parameters β_A and β_R, they are qualitatively affected by relatively large changes in β_A and β_R. For example, in Fig. 22 we show the calculated transition probabilities for the exponential-3 potential with $\beta_A = +0.05$, $\beta_R = +0.20$. This gives significantly poorer agreement with the experimental probabilities than $\beta_A = +0.06$, $\beta_R = +0.08$ (Fig. 21). When the VEP parametrization is used with $\beta_A = +0.05, \beta_R = +0.20$ the overall quality of the fit is also poorer than the results obtained with $\beta_A = +0.06, \beta_R = +0.09$ (Fig. 20), but not to the striking extent that was seen between Figs. 21 and 22. We therefore

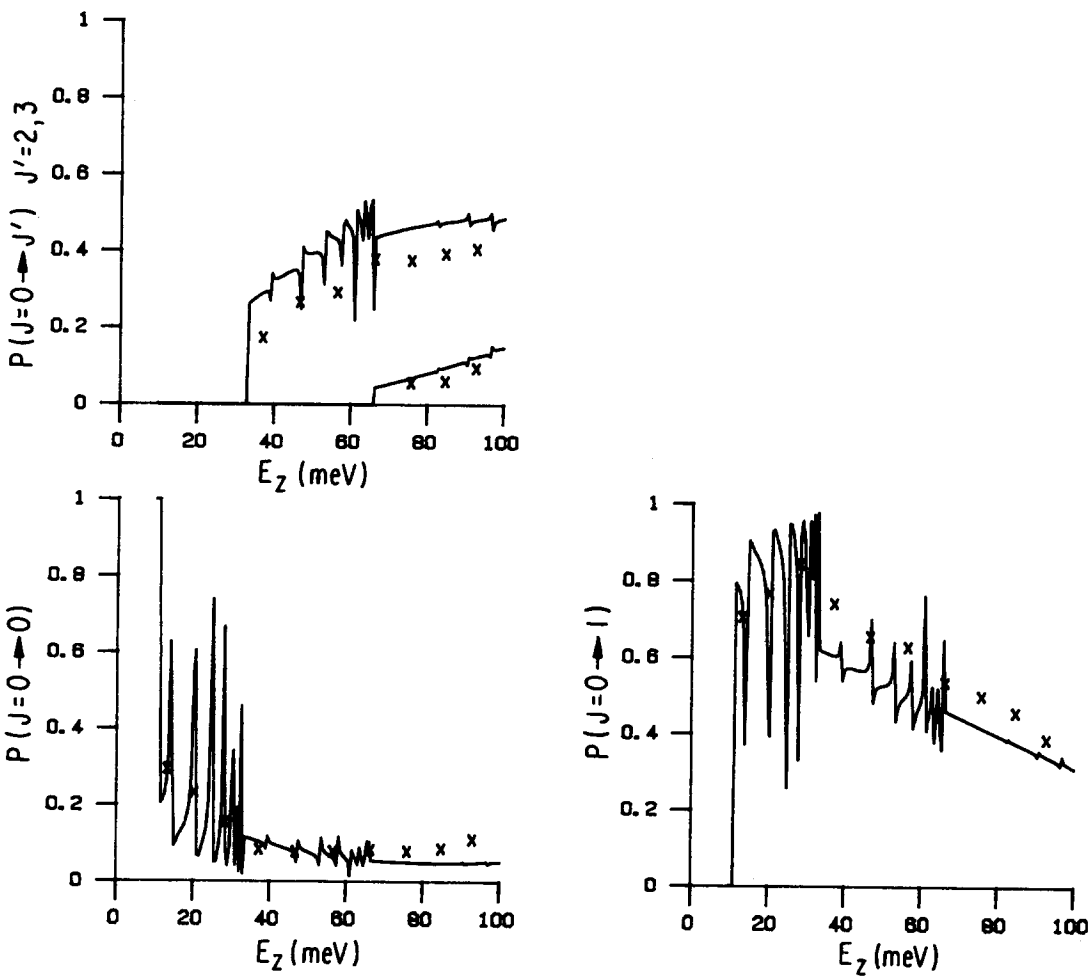

FIG. 20. Rotational transition probabilities $P(J = 0 \to J')$ $J' = 0,1,2,3$ as a function of E_z for HD, calculated using the VEP based potential with anisotropy parameters $\beta_A = +0.06, \beta_R = +0.09$. Potential parameters for $v_{00}^0(z)$ are given in Table II. Experimental transition probabilities are indicated by crosses (×).

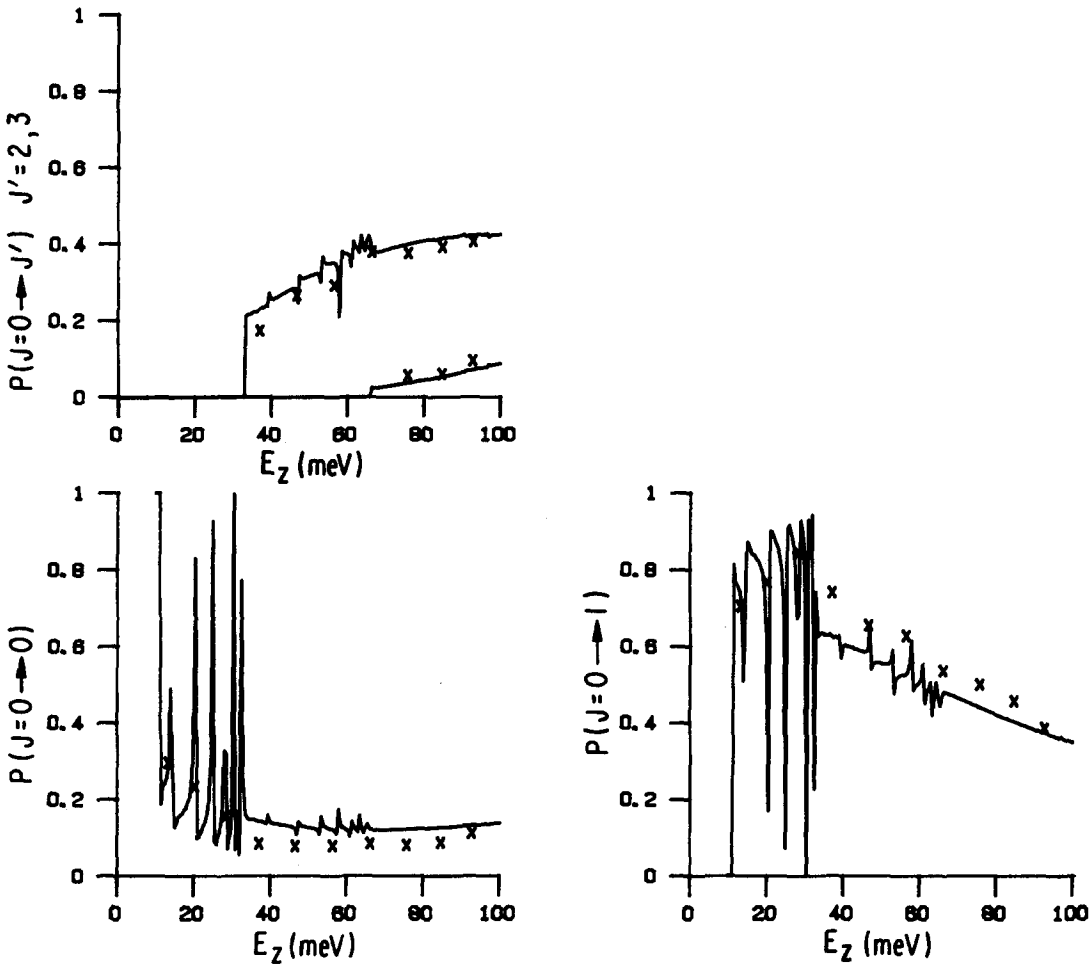

FIG. 21. Rotational transition probabilities $P(J=0\rightarrow J')\,J'=0,1,2,3$ as a function of E_z for HD, calculated using the exponential-3 based potential with anisotropy parameters $\beta_A = +0.06, \beta_R = +0.08$. Potential parameters for $v_{00}^0(z)$ are given in Table II. Experimental transition probabilities are indicated by crosses (×).

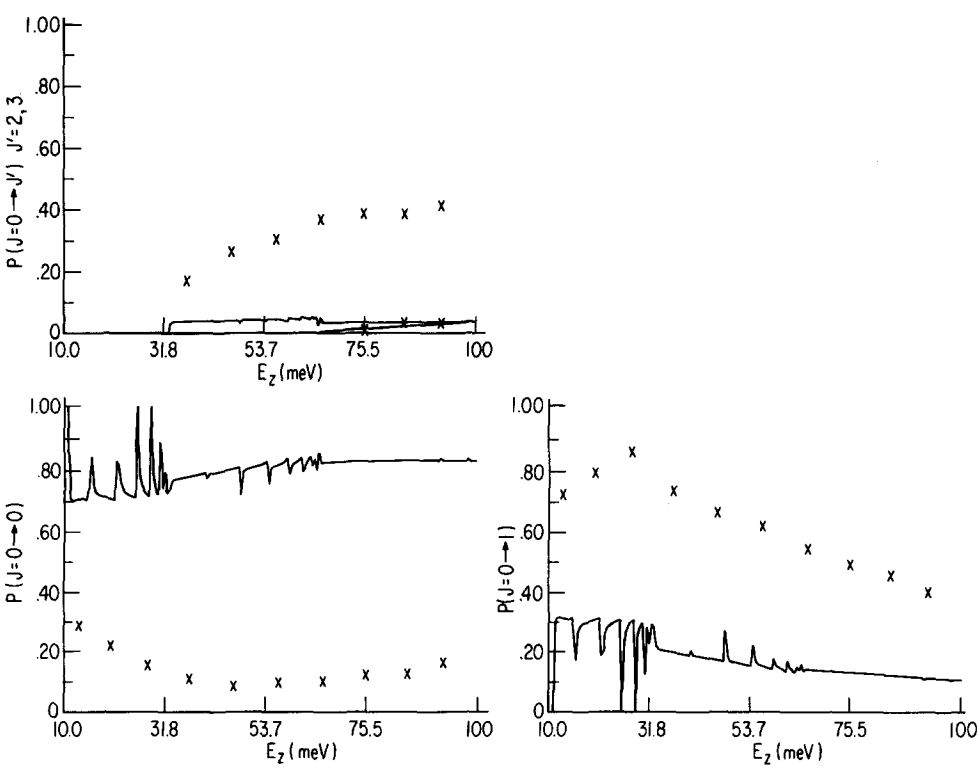

FIG. 22. Rotational transition probabilities $P(J=0\rightarrow J')\,J'=0,1,2,3$ as a function of E_z for HD, calculated using the exponential-3 based potential with anisotropy parameters $\beta_A = +0.05$, $\beta_R = +0.20$. Potential parameters for $v_{00}^0(z)$ are given in Table II. Experimental transition probabilities are indicated by crosses (×).

TABLE XI. Comparison of RMSA resonance energies for HD obtained by calculation, E^c, with the experimental resonance energies,[a] E^e.[b]

n, J	E^e	$\epsilon^{(0)}_{n,J}$	E^{c1}	E^{c2}	E^{c3}	E^{c4}	E^{c5}	E^{c6}
1,2	14.37	14.23	14.2	14.3	14.1	15.1	13.8	15.2
2,2	20.87	20.35	20.3	20.4	20.3	21.0	20.0	21.1
3,2	25.95	24.92	24.9	25.0	25.0	25.0	24.6	25.5
4,2	28.10	27.94	28.1	28.3	28.3	28.3	27.9	28.6
0,3	40.21	39.20	39.2	39.4	39.2	40.3	38.7	40.3
1,3	48.56	47.12	47.2	47.1	47.0	48.0	46.7	48.0
2,3	55.19	53.24	53.2	53.3	53.2	53.9	52.9	54.0
3,3	60.04	57.80	57.8	57.9	57.9	58.3	57.6	58.4
4,3	64.16	60.83	61.0	61.2	61.2	61.4	60.9	61.5

[a] Reference 9.

[b] Resonances are labeled n, J according to the bound state of $v^0_{00}(z)$ and rotor state J causing the resonance. Energies are given in terms of the normal component, E_z of the beam energy E_i in meV. E^{ci} refers to calculation i. Results are shown for seven calculations as follows: (1) $v^0_{00}(z) = \text{VEP}, \beta_A = +0.06, \beta_R = +0.09$; (2) $v^0_{00}(z) = \text{exp-3}, \beta_A = +0.06, \beta_R = +0.08$; (3) $v^0_{00}(z) = \text{exp-3}, \beta_A = +0.06, \beta_R = +0.09, \alpha_2 = +0.10$; (4) $v^0_{00}(z) = \text{VEP}, \beta_A = +0.05, \beta_R = +0.20$; (5) $v^0_{00}(z) = \text{VEP}, \beta_A = \beta_R = +0.10$; (6) $v^0_{00}(z) = \text{VEP}, \beta_A = \beta_R = -0.10$. The accuracy of the experimental measurements is ~3% (Ref. 9). All calculations were done on a grid of 0.1 meV in E_z.

see that even for HD, where the rotational inelasticity is largely dominated by the high mass asymmetry of the molecule, the energy dependence of the inelasticity can clearly distinguish between acceptable and unacceptable regions of the β_A, β_R parameter space.

Comparison of the calculated RMSA resonance energies with the experimentally measured values[9] is made in Table XI. The experimental values derived from the VEP potential, E^e, are compared here to the zeroth order BVRR energies derived from the VEP potential, $E^{(0)}$, and to the exact resonance energies E^{ci} derived from six parametrizations i of the potential $V_{00}(z,\theta)$: (1) VEP; $\beta_A = +0.06$, $\beta_R = +0.09$; (2) exp-3; $\beta_A = +0.06$, $\beta_R = +0.08$; (3) exp-3; $\beta_A = +0.06$, $\beta_R = +0.09$, $\alpha_2 = +0.10$; (4) VEP; $\beta_A = +0.05$, $\beta_R = +0.20$; (5) VEP; $\beta_A = \beta_R = +0.10$; (6) VEP; $\beta_A = \beta_R = -0.10$. The results from potentials (1), (2), and (3) which all have anisotropic parametrization in the region of our previous conclusions derived from H_2 and D_2, differ by at most 0.2 meV, which is the magnitude of the experimental precision. Comparing to the experimental resonance energies, with the exception of the three highest energy resonances for adsorbed $J = 3$, the calculated energies fall within 0.2 meV or less of the experimental values. The $J = 3$, $n = 3,4$ resonances are predicted to be too low by several meV for all parametrizations shown; this was seen for all combinations β_A, β_R probed in Figs. 7 and 8. Comparing now with results from potential (4) ($\beta_A = +0.05$, $\beta_R = +0.20$), we see very similar behavior. As discussed in Sec. II, the RMSA resonance energies are strongly dominated by the anisotropy arising from the molecular asymmetry. In contrast to the energy dependence of the HD rotational transition probabilities, it is not possible to distinguish between these two regions of β_A, β_R parameter space from the RMSA resonance positions.

As a final comparison we have also included in Table XI the resonance energies predicted by the single β parametrization ($\beta = \beta_A = \beta_R$), potentials (5) and (6). These show that both the sign and magnitude of the shift depend on the sign of β. It is interesting that the value of $\beta = -0.10$ gives approximately the same shifts as $\beta_A = +0.05$, $\beta_R = +0.20$, an observation which can be rationalized in terms of the relative sizes of the expectation values of $v_{00,R}(z)$ and $v_{00,A}(z)$.[25] This equivalence of the RMSA shifts is to be contrasted with the very different behavior seen for the H_2 rotational transition probability ratios for these two anisotropic parametrizations, within the VEP based form of $V_{00}(z,\theta)$. Such an observation demonstrates once again the need to analyze *both* transition probabilities and resonance energies in order to extract unambiguous information about the anisotropic parameters.

VII. SUMMARY AND CONCLUSION

In this paper we have investigated the anisotropic component of the laterally averaged interaction potential, $V_{00}(z,\theta)$, for molecular hydrogen/Ag(111), by employing a combination of experimental measurements and theoretical calculations. The calculations utilized a laterally averaged potential which was expanded in a Legendre series for a symmetric (homonuclear) system, Eqs. (2.5) and (2.6), in which the anisotropic component was given by a two parameter model, Eq. (2.8). This two parameter representation of $v^2_{00}(z)$ allowed us to systematically examine the orientation dependence of both the attractive and repulsive parts of the potential. A three parameter model of $v^2_{00}(z)$ was also briefly examined which allowed the softness of the repulsive component of $v^2_{00}(z)$ to be independently varied. The isotropic potential used in these calculations was represented by variable exponent and exponential-3 parametrizations, Eqs. (2.9)–(2.11), that were previously shown to reproduce the experimental bound state resonance spectra for p-H_2 and o-D_2 on Ag(111).[6,10] The exponential-3 potential was used to a greater extent in our analysis than the variable exponent potential as it has the proper form predicted by *ab initio* calculations.

Our analysis began by comparing experimentally derived rotationally inelastic transition probabilities, taken as a function of collision energy normal to the surface, with those

resulting from close coupled quantum scattering calculations. Extensive iterations of the anisotropy parameters β_A and β_R in these calculations revealed that the energy dependent H_2 and D_2 transition probabilities fall along a *common* band of β_A, β_R values (Figs. 7 and 8), with small β_R correlating with small β_A. Comparable results were found using the VEP and exponential-3 isotropic potentials, with the exponential-3 results showing slightly better agreement with the transition probabilities as a function of energy. When β_A is a set at the theoretical value predicted by Harris and Feibelman,[12] $\beta_A = 0.06$, a β_R value of 0.09 is found for the VEP parametrization of $v_{00}^0(z)$, and $\beta_R = 0.08$, for the exponential-3 based potential. These values for β_R are in good agreement with the *ab initio* result for H_2/Cu(100) given by Harris and Liebsch,[13] $\beta_R \sim 0.08$, but are smaller than the value calculated by Norlander and Holmberg, $\beta_R \sim 0.18$.[24] Inclusion of an additional exponentially decaying term in the repulsive anisotropic potential causes some improvement between the energy dependence of the experimental and calculated probabilities to be realized. For example, an exponential-3 based potential which includes this additional softness parameter gives a better fit to the data with $\beta_A = 0.06, \beta_R = 0.09$, and $\alpha_2 = 0.10$ than was originally obtained with $\beta_A = 0.06$, $\beta_R = 0.08$, and $\alpha_2 = 0.00$. We also note that the transition probabilities for the homonuclear hydrogen isotopes are quite sensitive to changes in β_A and β_R, and can therefore be used to distinguish between different regions of the β_A, β_R parameter space. This was demonstrated in Fig. 11, where the H_2 rotational transition probabilities calculated with $\beta_R \sim 0.20$ were found to be in poorer agreement with the data than those calculated using $\beta_R \sim 0.09$ (especially for the exponential-3 potential).

The DSA resonance energies for p-H_2 and n-H_2 were then analyzed in order to examine how the magnetic sublevel splittings for $J = 1$ n-H_2 evolve as a function of β_A, β_R and bound level n. Unfortunately, distinct splittings have not been observed in our DSA data for either n-H_2 or n-D_2 on Ag(111).[6,10] This can be attributed to the *extremely* weak nature of the diffractively coupled resonances which are observed on Ag(111), a closest packed metallic surface, and to the finite energy resolution of our instrument. However, the $n = 2\binom{10}{01}$ resonance for n-H_2 along the $\langle 11\bar{2}\rangle$ direction exhibited reproducible linewidth broadening relative to p-H_2, and was examined using a detailed forward convolution procedure. The results of this analysis, given as a function of β_A and β_R in Fig. 8, intersect the rotationally inelastic H_2 data at $\beta_A \sim 0.06, \beta_R \sim 0.08$. Although the quantitative information derived from this line shape analysis pertaining to the anisotropic potential is the least definitive evidence presented in this paper (due to extensive convolutions and low signal level), it does serve to demonstrate that this type of experiment can be used to examine $v_{00}^2(z)$ in a manner complementary to inelastic scattering. However, we wish to strongly emphasize that the calculated energy level shifts for the $|J,m\rangle = |1,0\rangle$ and $|1,\pm 1\rangle$ states relative to $|0,0\rangle$ depend not only on the values of β_A and β_R, i.e., on the anisotropic potential, but also on the parametric form of $v_{00}^0(z)$, the laterally averaged isotropic potential. This is demonstrated in Table VIII, where the shifts for $J = 1$ n-H_2 exhibit an obvious dependence on the isotropic potential used in the calculation.

Finally, the β_A and β_R values determined in the H_2 and D_2 experiments were used to calculate rotational transition probabilities and RMSA resonance positions for HD incident upon Ag(111) modeled as a flat surface. These calculated values were then compared to our experimental results. We find that although the rotationally inelastic transition probabilities and RMSA resonance energies for HD are relatively insensitive to small changes in the anisotropy of the potential, the results tend to support the conclusions drawn from the H_2 and D_2 experiments. In particular, the rotationally inelastic scattering results for HD differentiate between the $\beta_A = 0.06, \beta_R = 0.09$ and $\beta_A = 0.05, \beta_R = 0.20$ parameter sets, with the former giving substantially better agreement to the data. This can be seen for the exponential-3 based potential in Figs. 21 and 22. In contrast to this, the HD RMSA resonance energies are found to exhibit very similar J-dependent level shifts using the $\beta_A = 0.06, \beta_R = 0.09$ and $\beta_A = 0.05, \beta_R = 0.20$ parameter sets. This surprising insensitivity to the anisotropic potential arises for the heteronuclear isotope since the RMSA resonance energies are strongly dominated by the molecular asymmetry of this system.

In conclusion, we believe this investigation has demonstrated that in order to make an accurate and unambiguous determination of a molecule–surface potential, a wide combination of complementary measurements and calculations are needed. Diffractive selective adsorption and thermal desorption measurements can be used to examine the orientation independent part of the potential, as was done in our first paper of this series on hydrogen/Ag(111).[10] Diffraction and diffraction-rotation measurements can probe the periodic part of the potential, as will be discussed in a future publication.[11] Finally, as demonstrated in this paper, rotationally inelastic scattering, and selective adsorption resonances which exhibit J and m dependent level shifts, can be used to examine the anisotropic part of the potential. Using this combination of experimental measurements and calculations we have determined attractive and repulsive anisotropy parameters which agree well with calculated values.[12,13] This paper, together with the previous one dealing with the isotropic potential, provides one of the most comprehensive studies of a low energy molecule–surface potential to date.

ACKNOWLEDGMENTS

The authors wish to thank K. D. Gibson and Y. W. Yang for their assistance during the course of this work, and J. P. Cowin for his participation in the HD RMSA study, Ref. 9. This work was supported, in part, by the Office of Naval Research (ONR-N00014-77-C-0240), by the National Science Foundation (NSF-CHE-8203453), by the Materials Research Laboratory Program at the University of Chicago (NSF-DMR-7924007), and by a Camille and Henry Dreyfus Young Faculty Grant to S. J. Sibener.

[1]H. Hoinkes, Rev. Mod. Phys. **52**, 933 (1980); J. Perreau and J. Lapujoulade, Surf. Sci. **122**, 341 (1982).
[2]M. J. Cardillo, Annu. Rev. Phys. Chem. **32**, 331 (1981).

[3]A. C. Luntz, A. W. Kleyn, and D. J. Auerbach, Phys. Rev. B **25**, 4273 (1982).
[4]Ph. Avouris, D. Schmeisser, and J. E. Demuth, Phys. Rev. Lett. **48**, 199 (1982).
[5]S. Andersson and J. Harris, Phys. Rev. Lett. **48**, 545 (1982).
[6]C. F. Yu, K. B. Whaley, C. S. Hogg, and S. J. Sibener, Phys. Rev. Lett. **51**, 2210 (1983).
[7]M. Chiesa, L. Mattera, R. Musenich, and C. Salvo, Surf. Sci. **151**, L145 (1985).
[8]J. P. Cowin, C. F. Yu, S. J. Sibener, and J. E. Hurst, J. Chem. Phys. **75**, 1033 (1981).
[9]C. F. Yu, C. S. Hogg, J. P. Cowin, K. B. Whaley, J. C. Light, and S. J. Sibener, Isr. J. Chem. **22**, 305 (1982).
[10]C. F. Yu, K. B. Whaley, C. S. Hogg, and S. J. Sibener, J. Chem. Phys. **83**, 4217 (1985).
[11]K. B. Whaley, C. F. Yu, C. S. Hogg, J. C. Light, and S. J. Sibener (to be published).
[12]J. Harris and P. J. Feibelman, Surf. Sci. **115**, L133 (1982).
[13]J. Harris and A. Liebsch, Phys. Scr. T **4**, 14 (1983).
[14]W. Kolos and L. Wolniewicz, J. Chem. Phys. **46**, 1426 (1967).
[15]L. Mattera, C. Salvo, S. Terreni, and F. Tommasini, Surf. Sci. **97**, 158 (1980).
[16]See, for example, E. Ghio, L. Mattera, C. Salvo, F. Tommasini, and U. Valbusa, J. Chem. Phys. **73**, 556 (1980).
[17]K. A. Rieder and N. Garcia, Phys. Rev. Lett. **49**, 43 (1982).
[18]K. B. Whaley, J. C. Light, J. P. Cowin, and S. J. Sibener, Chem. Phys. Lett. **89**, 89 (1982).
[19]R. Schinke, V. Engel, and H. Voges, Chem. Phys. Lett. **104**, 279 (1984).
[20]G. A. Parker, T. G. Schmalz, and J. C. Light, J. Chem. Phys. **73**, 1757 (1980).
[21]C. A. Becker, Ph.D. thesis, University of Chicago, 1980.
[22]J. P. Cowin, C. F. Yu, S. J. Sibener, and L. Wharton, J. Chem. Phys. **79**, 3537 (1983).
[23]J. Andres, U. Buck, F. Huisken, J. Schleusener, and F. Torello, J. Chem. Phys. **73**, 5620 (1980).
[24]P. Nordlander and C. Holmberg (to be published).
[25]K. B. Whaley, Ph.D. thesis, University of Chicago, 1984.